Journal of Geophysical Research: Space Physics

RESEARCH ARTICLE
10.1002/2017JA025140

Key Points:
- MARSIS AIS/Mars Express shows magnetically controlled density structures in the dayside Martian ionosphere
- Time series of electron density profiles corrected for dispersion are used to find the shape of 48 structures
- The majority of these structures are bulges, and a few are of other simple shapes: dip, downhill slope, and uphill slope

Correspondence to:
C. Diéval,
cdieval05@gmail.com

Citation:
Diéval, C., Kopf, A. J., & Wild, J. A. (2018). Shapes of magnetically controlled electron density structures in the dayside Martian ionosphere. *Journal of Geophysical Research: Space Physics*, *123*, 3919–3942. https://doi.org/10.1002/2017JA025140

Received 18 DEC 2017
Accepted 18 MAR 2018
Accepted article online 22 MAR 2018
Published online 2 MAY 2018

Shapes of Magnetically Controlled Electron Density Structures in the Dayside Martian Ionosphere

C. Diéval[1], A. J. Kopf[2], and J. A. Wild[1]

[1]Department of Physics, Lancaster University, Lancaster, UK, [2]Department of Physics and Astronomy, University of Iowa, Iowa City, IA, USA

Abstract Nonhorizontal localized electron density structures associated with regions of near-radial crustal magnetic fields are routinely detected via radar oblique echoes on the dayside of Mars with the ionospheric sounding mode of the Mars Advanced Radar for Subsurface and Ionospheric Sounding (MARSIS) radar onboard Mars Express. Previous studies mostly investigated these structures at a fixed plasma frequency and assumed that the larger apparent altitude of the structures compared to the normal surrounding ionosphere implied that they are bulges. However, the signal is subjected to dispersion when it propagates through the plasma, so interpretations based on the apparent altitude should be treated with caution. We go further by investigating the frequency dependence (i.e., the altitude dependence) of the shape of 48 density structure events, using time series of MARSIS electron density profiles corrected for signal dispersion. Four possible simplest shapes are detected in these time series, which can give oblique echoes: bulges, dips, downhill slopes, and uphill slopes. The altitude differences between the density structures and their edges are, in absolute value, larger at low frequency (high altitude) than at high frequency (low altitude), going from a few tens of kilometers to a few kilometers as frequency increases. Bulges dominate in numbers in most of the frequency range. Finally, the geographical extension of the density structures covers a wide range of crustal magnetic fields orientations, with near-vertical fields toward their center and near-horizontal fields toward their edges, as expected. Transport processes are suggested to be a key driver for these density structures.

1. Introduction

The Martian upper atmosphere is not currently protected by a global magnetic dipole and is therefore exposed to erosion by the incoming supersonic solar wind. An induced magnetosphere arises from the interaction between the conductive ionospheric obstacle and the solar wind plasma with its embedded interplanetary magnetic field (IMF) (e.g., Nagy et al., 2004). In addition, localized crustal magnetic fields (e.g., Acuña et al., 1999), remnants of a past Martian dynamo, are able to stand off the solar wind and locally control the magnetic topology at low altitudes in the forms of magnetic arcades with both foot points anchored in the planetary crust (closed field lines), while in other areas the IMF is free to reach lower altitudes, imposing a mostly horizontal induced magnetic field on the dayside (e.g., Brain et al., 2003). The magnetic anomalies form minimagnetospheres, which rotate with the planet, locally regulating atmospheric loss (e.g., Ramstad et al., 2016).

The Mars Advanced Radar for Subsurface and Ionospheric Sounding (MARSIS) experiment (Picardi et al., 2004) is part of the payload onboard the Mars Express (MEX) orbiter. MEX orbit has a period of 7.5 hr and inclination ~86° around Mars, with periapsis at ~300 km and apoapsis at ~10,000 km. MARSIS is able to run in either a subsurface mode or an active ionosphere sounding (AIS) mode. In the latter mode, which we are interested in here, the radar has provided numerous observations of the Martian ionosphere since August 2005 (e.g., Morgan et al., 2008; Němec et al., 2010; Sánchez-Cano et al., 2016). During topside sounding, a 40-m tip-to-tip dipole antenna sweeps through a frequency table (160 steps from 0.1 to 5.4 MHz, with resolution $\Delta f/f \approx 2\%$) during 1.26 s by transmitting 91.4-μs long sinusoidal pulses in a broad angular interval centered on nadir. The radio waves at a given frequency propagate, affected by dispersion (including varying group velocity and raypath bending), through the plasma layers of increasing plasma frequency until the local plasma frequency matches the pulse frequency, at which reflection occurs. Pulse reflection back to the radar nominally occurs at normal angle to the plasma layer. Two types of echoes can be detected at the same time: vertical echoes that reflect from the ionosphere below MEX (assumed to be ideally horizontally stratified) and oblique echoes that reflect from nearby nonhorizontal density structures. The receiver measures the time delay for receiving the echo, in 80 bins of duration 91.4 μs starting 253.9 μs and ending 7.56 ms after the start

of the pulse. Full-frequency sweeps are repeated at 7.54 s cadence. The basic measurement unit is a matrix of received power spectral density versus time delay and frequency, called an ionogram. In this mode, the topside sounder samples plasma layers of increasing density as altitude decreases, from the spacecraft down to the ionospheric peak, according to the relationship $f_p = 8980\sqrt{N_e}$ between electron density N_e in cm^{-3} and plasma frequency f_p in Hz.

This study focuses on localized density structures associated with regions of near-radial crustal magnetic fields, detected by MARSIS via oblique echoes, in the dayside Martian ionosphere (Andrews et al., 2014; Diéval et al., 2015; Duru et al., 2006; Gurnett et al., 2005; Nielsen, Wang, et al., 2007; Venkateswara Rao et al., 2017). When the spacecraft moves toward or away from such reflecting target, two echoes (one vertical and one oblique) are received, with the time separation between the echoes either decreasing or increasing. When the spacecraft passes directly over the structure, only one echo is detected; the echo may be vertical or oblique depending on the inclination of the plasma layer at each reflection point along the structure. This behavior is characterized by downward facing hyperbola signatures in echograms, which are displays of received intensity at a fixed frequency as function of time and echo range. In echograms, one can usually see that for a given frequency, the apex of the hyperbola appears to stand at or above the surrounding normal ionosphere (root-mean-square [rms] 19 km higher at a fixed frequency 1.8 MHz according to Duru et al., 2006). The apparent altitude of the ionospheric echoes is calculated as the spacecraft altitude minus the echo range assuming speed of light in a vacuum. Gurnett et al. (2005) and Duru et al. (2006) exploited the higher apparent altitude of these structures to interpret them as bulges. Such plasma layers are inclined at a range of angles to the horizontal, up to 90° (Nielsen, Wang, et al., 2007). In addition, Venkateswara Rao et al. (2017) reported that the main ionospheric layer and the topside layers at higher altitude (topside layers discovered by Kopf et al., 2008, in the MARSIS data) may both cause oblique echoes in areas of near-radial crustal fields, indicating that the density contours of these topside layers can also be tilted.

The density structures have regularly been observed over periods of tens of days through subsequent MEX passes above the same magnetized areas, even though the upstream conditions were changing, indicating long-term stability (Andrews et al., 2014). They occur above the strong magnetic anomalies of the southern hemisphere as well as above the weak magnetic anomalies of the northern hemisphere, and their latitude extent matches rather well with the latitude extent of areas of near-radial fields of a given polarity (upward or downward oriented) (Diéval et al., 2015). It is therefore inferred that these structures are not single points but are spatially extended and confined by the areas of magnetic cusps, reaching horizontal sizes of a few hundreds of kilometers along the spacecraft footprint (Diéval et al., 2015). Oblique echoes are found in regions that have statistically low to moderate rates (20–50%) of open field lines (field lines with one footprint in the crust and the other connected to the IMF) (Diéval et al., 2015). This indicates that their regular occurrence does not depend on the infrequent magnetic reconnection between the crustal fields that rotate with the planet and the variable IMF. In addition, Diéval et al. (2015) reported simultaneous in situ observations of suprathermal electron distributions by the Electron Spectrometer (Barabash et al., 2006) onboard MEX, which indicated that the plasma regime (ionosphere or shocked solar wind) at the location of MEX (depending on the spacecraft position relative to plasma boundaries) had no influence on the observability of oblique echoes. Solar wind electron precipitation depends on the time-dependent magnetic reconnection between near-radial crustal fields and IMF to reach low altitudes along open field lines (which would otherwise be closed at other times; see e.g., Brain et al., 2007).

These recent results do not support the hypothesis proposed by earlier studies (Duru et al., 2006; Gurnett et al., 2005) that solar wind precipitation into magnetic cusps is the primary driver of these density structures. Gurnett et al. (2005) and Duru et al. (2006) had suggested that the solar wind penetrating to low altitude along open field lines would ionize and heat the neutrals, the latter causing an inflation of the neutral atmosphere (which moves additional extreme ultraviolet-ionizable material to higher altitude), such as to generate electron density bulges.

Other formation mechanisms have been proposed. If solar wind precipitation is involved, the resulting increase in electron temperature at the altitude of energy deposition causes a reduction of the ion-electron recombination rate, which increases the plasma density (Andrews et al., 2014). Another source of temperature increase may be Joule heating from field-aligned currents and Pedersen currents in regions of magnetic cusps (Fillingim et al., 2010, 2012; Riousset et al., 2013, 2014; Withers et al., 2005). Finally, a 2-D ionospheric

model taking plasma transport into account (Matta et al., 2015) has shown that an expanded ionosphere may form in regions of vertical crustal fields via upward diffusion, because it is easier for plasma to move along field lines than across them.

The previous studies of oblique echoes were carried out at a fixed frequency, though Nielsen, Wang, et al. (2007) reported that during simultaneous observations of vertical and oblique echoes, the maximum frequency of the oblique echo was often smaller than the maximum frequency of the vertical echo. This was interpreted as off-nadir reflections from density structures more tilted to the vertical at low frequencies than at high frequencies. However, there has been no systematic study of the frequency variation of the density structures so far. Since low frequencies correspond to high altitudes and high frequencies to low altitudes, the variations of these structures with altitude remain ambiguous. Also, it has been previously assumed that the oblique echoes are reflected from bulges, because a given electron density level stands at a higher apparent altitude than the surrounding ionosphere. But, the apparent altitude estimation assumes that the pulse propagates at the speed of light in vacuum c, that is, without correction for dispersion effects in the ionosphere. However, radio waves of frequency f will propagate with a group velocity V_g through an ionized medium of varying refractive index $n = \sqrt{1 - \left(\frac{f_p}{f}\right)^2}$. The group velocity $V_g = c\,n = c\sqrt{1 - \left(\frac{f_p}{f}\right)^2}$ is less than the speed of light and becomes vanishingly small when f approaches f_p, at which signal reflection occurs. For a given time delay, the apparent range of the echo is therefore an upper limit for the real range. Correcting the altitude for dispersion confirms whether or not the density structures really stand higher than the surrounding ionosphere, and by how much.

The aim of the current work is to determine the correct shape and magnitude of the altitude changes across the structures as a function of frequency, and thus as a function of altitude, from the high densities near the ionospheric peak down to the lowest densities measurable by the topside sounding technique. This information may provide insight into the formation processes of the density structures.

The structure of the paper is as follows: the method is described in section 2; the results are presented in section 3 (divided into three sections: close look at individual events [section 3.1], statistics [section 3.2], and influence of crustal magnetic field orientation [section 3.3]) and discussed in section 4. Finally, we summarize in section 5.

2. Method

Examples of hyperbola signatures from three density structures are shown in Figure 1. The time series runs from 13:00 to 13:15 universal time (UT) on 22 July 2006, orbit 3253. During the pass, MEX traveled above moderate strength magnetic anomalies from 46° to −9° latitude at a nearly fixed E longitude of 350°, inbound toward periapsis (periapsis at 324 km altitude at 13:03:45 UT) and then outbound, on dayside. The altitude varied from 362 to 709 km and the solar zenith angle (SZA) varied from 33° to 48°. Figure 1a shows the crustal magnetic field model of Cain et al. (2003) evaluated at 150 km altitude at MEX footprint, with the magnetic zenith angle (left axis, black curve) and the magnetic field strength (right axis, red curve). The magnetic zenith angle is the angle of the magnetic field vector relative to the zenith: 0° is vertical upward, 90° is horizontal. Figures 1b–1e show MARSIS echograms at four frequencies: 1.52, 1.979, 2.548, and 3.03 MHz, equivalent to electron densities of 2.86×10^4, 4.86×10^4, 8.05×10^4, and 1.14×10^5 cm^{-3}, at the reflection point, respectively. The vertical axis is the apparent altitude and the color codes the received intensity.

In all echograms, the vertical echo from the assumed ideally horizontally stratified ionosphere is identified as the bright yellow-red trace at near-constant apparent altitude (varying from 100 down to 50 km as frequency increases). At frequency 1.52 and 1.979 MHz (Figures 1b and 1c), three hyperbola signatures are visible, with apexes at 13:03:08, 13:08:39, and 13:12:03 UT. The signatures are marked with black ellipses. At 150 km altitude, the modeled field strength and magnetic zenith angle for these structures are 109 nT and 166° at 13:03:08 UT, 194 nT and 12° at 13:08:39 UT, and 48 nT and 45° at 13:12:03 UT (Figure 1a). So these density structures are located in regions of near-vertical to oblique crustal fields, consistent with previous reports (e.g., Gurnett et al., 2005). We note that the oblique echoes tend to be more pronounced at low frequencies than at high frequencies. Indeed, there is only one hyperbola signature visible at 2.548 and 3.03 MHz

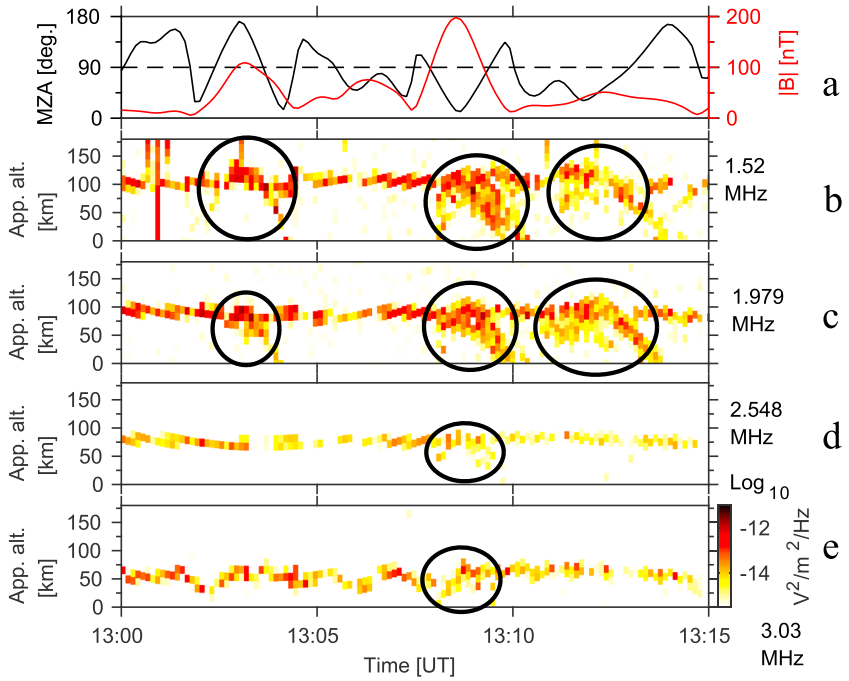

Figure 1. Time series on 22 July 2006, 13:00–13:15 UT, orbit 3253. (a) Crustal magnetic field calculated at 150 km altitude at MEX footprint using the Cain et al. (2003) model: magnetic zenith angle (black curve, left axis) and magnetic field strength (red curve, right axis). The horizontal black dashed line marks the 90° angle (horizontal orientation). (b–e) MARSIS echograms at four sounding frequencies: 1.52 (b), 1.979 (c), 2.548 (d), and 3.03 MHz (e); the vertical axis shows the apparent altitude, and the color coding shows the received signal spectral density. The black ellipses mark the hyperbola signatures associated to oblique echoes.

(Figures 1d and 1e). This indicates that the density contours are more inclined for low densities than for high densities, and therefore more able to give oblique echoes, in agreement with Nielsen, Wang, et al. (2007).

We have conducted a statistical study of a list of oblique echoes previously examined by Andrews et al. (2014) and Diéval et al. (2015). The original list from Andrews et al. (2014) contains 1,126 events, detected when MEX was on dayside (SZA $< 90°$) with an altitude $<$1,100 km, spanning August 2005 to February 2013. The limit at 1,100 km comes from the maximum range for which MARSIS can receive ionospheric reflections due to the time delay measurement window. The present study considers 1,066 events from this list for which the hyperbola apexes stand at or above the surrounding ionosphere, as determined by Diéval et al. (2015). This ensures that we only look at density structures found directly below the spacecraft. We examine the density structures as a function of frequency (i.e., as a function of altitude); for convenience we need to look at all events in the same frequency bins, so we keep data starting from 1 October 2005, after which the MARSIS frequency table became fixed: we keep 901 events from the previous list. It is convenient to work with frequencies here because the altitude of a plasma layer at a given frequency depends on many factors, including SZA, extreme ultraviolet intensity, strength and orientation of local magnetic field, and distance of the planet from the Sun.

The difference in apparent altitude between the hyperbola apexes and the normal surrounding ionosphere is usually positive and of the order of 19 km (e.g., Duru et al., 2006), which led to the assumption that the density structures are bulges. We want to check this assumption with the altitude measurement corrected for dispersion. The measured time delays $\Delta t(f)$ as a function of frequency can be inverted to obtain the frequency (and density) profile as a function of corrected altitude $z(f_p)$, referred to as the electron density profile (EDP). The Abel transformation gives the solution $z(f_p) = \frac{2}{\pi}\int_{\alpha_0}^{\frac{\pi}{2}} c\Delta t(f_p \sin\alpha)d\alpha$ (Budden, 1961), where $\sin\alpha_0 = \frac{f_p(\mathrm{SC})}{f_p(\mathrm{max})}$. The integration in frequency goes from the local plasma frequency at the spacecraft f_p(SC) to the maximum plasma frequency of the ionosphere f_p(max).

There are several challenges associated to the detection of the ionospheric reflection at low frequencies, and thus to their inversion. The local plasma frequency is obtained from the MARSIS plasma oscillations excited in the antenna (e.g., Gurnett et al., 2005). These harmonics, recognizable as vertical bright stripes in MARSIS

ionograms, make the estimation of reflection time delays more difficult at low frequencies. Electron cyclotron harmonics are also detected as horizontal bright stripes in MARSIS ionograms, when MARSIS is exposed to local magnetic fields of strength larger than a few tens of nanotesla (Gurnett et al., 2005); these interferences again hinder the visibility of the ionospheric echo at low frequencies (the problem is even more acute above the magnetic anomalies, where we conduct the present work). Finally, the transmitted power falls off sharply at low frequencies, which makes the reflected signal often too low to be detectable at frequencies $<$ ~1 MHz (e.g., Morgan et al., 2013). These circumstances of low signal-to-noise ratio lead to a data gap between the local plasma frequency measured at MEX location and the lowest frequency measurable with the ionospheric reflection. The error on the determination of the corrected altitude becomes large if the frequency range of the gap is significant compared to the frequency range of the reflection (e.g., Morgan et al., 2013).

The density profiles presented here were obtained with the inversion method by Němec, Morgan, and Gurnett (2016), itself derived from the standard inversion method by Morgan et al. (2013). The inversion process in these methods assumes that the pulse propagates along the nadir direction (vertical echo), the ionosphere has plane-parallel stratification, there are no magnetic effects, and the density profile monotonically increases as altitude decreases. We note that the existence of nonmonotonic density profiles with transient topside layers above the main density peak, for which the assumption of monotonic profiles is not valid (e.g., Kopf et al., 2008). Also, the plane-parallel approximation breaks down near the terminator, where the plasma density is weaker and more variable than on dayside (e.g., Fox & Yeager, 2006; Gurnett et al., 2005). In addition, near the terminator, MARSIS sometimes detects ionospheric echoes and ground echoes overlapping for a range of frequencies, which can be explained by the strong horizontal density gradients present at the terminator (Duru, Morgan, & Gurnett, 2010). In this case, a single ionospheric reflection is observed, which is not vertical, but off-nadir. Finally, the lower densities near the terminator or at high spacecraft altitude increase the frequency range of the data gap compared to the measured frequency range of the ionospheric reflection, making the inversion process more error-prone.

For these reasons, Morgan et al. (2013) considered EDPs as unreliable for SZA $>$85° or spacecraft altitude $>$800 km. In practice, this means that they rejected profiles for which the frequency range of the gap is larger than the frequency range of the ionospheric echo and/or larger than 1 MHz. In addition, Morgan et al. (2013) have excluded profiles with ionospheric peak frequencies between 2.25 and 2.3 MHz, for which there is a sensitivity gap. Since the terminator region causes many difficulties, we restrict our study to SZA $<$85°: this leaves 890 events to study. The major difference between the two mentioned inversion methods is the functional form used for $f_p(z)$ in the low-frequency data gap. The reader is directed to Němec, Morgan, and Gurnett (2016) for details.

Finally, one may question whether the assumptions of vertical reflection and plane-parallel stratification are reasonable in regions of density structures (with inclined density layers). We discuss the problem and make a check of these assumptions in Appendix A. The conclusion of this check is that for the events investigated in this work, the assumption of plane-parallel stratification is definitively good, and the assumption of vertical propagation is good enough to use as an approximation. Therefore, we trust that these EDPs are appropriate for this study.

We want to look at time series of EDPs for each density structure, by selecting all available EDPs (from the processing by Morgan et al., 2013) during the period for which the spacecraft passes overhead the structure. For this purpose, we need the echograms, which we integrate over a range of frequencies typical for oblique echoes (we chose between 1.8 and 2 MHz), rather than just taking one frequency level, because it improves the signal-to-noise ratio of the echogram (less background noise and more pronounced ionospheric traces, resulting from combining different frequencies) and shows ionospheric features that could possibly be missed if using only one frequency level. This period of overhead pass is estimated from the MARSIS echograms by considering the time at which the hyperbola signature starts merging and then stops merging with the main surrounding ionosphere echo. This exercise is a rough estimate (but good enough for our purpose) because of the following difficulties. (1) The merging time for each hyperbola leg can take the duration of several ionograms (several times 7.54 s) and is thus not instantaneous or easy to determine. (2) Several structures can be superposed on top of each other due to the frequent occurrence of oblique echoes in neighboring regions of alternating radial field polarities; this makes it difficult to separate individual structures. (3) The structure can present only one clear leg or present one or two short/unclear legs, which make it hard to

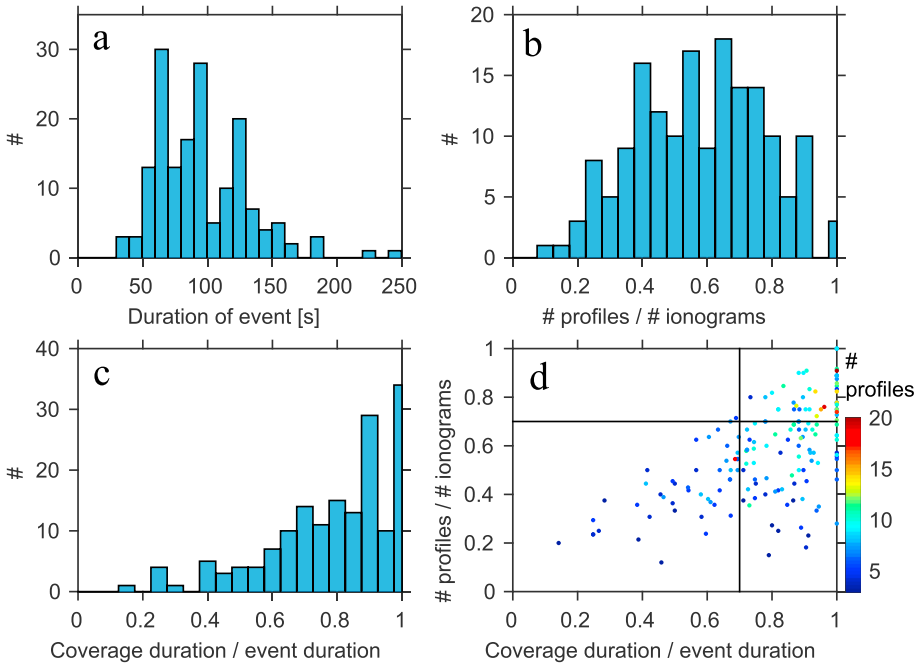

Figure 2. (a) Distribution of event duration for all the events. (b) Distribution of the number of available EDPs divided by the number of ionograms during the duration of each event (ratio of numbers), for all the events. (c) Distribution of the duration of EDP coverage divided by the event duration of each event (ratio of durations), for all the events. (d) Scatter plot of the ratio of durations versus the ratio of numbers, colored by the number of available EDPs during the duration of each event, for all the events. The black solid vertical and horizontal lines are plotted for abscissa = 0.7 and ordinate = 0.7, respectively. We keep the 48 events for which number of available EDPs divided by the number of ionograms ≥0.7 and duration of the EDP coverage divided by the event duration ≥0.7.

determine where are the edges of the structure. (4) In practice, the period of overhead pass is itself limited by the coverage of available EDPs during this period. From the previous list, there are 165 events for which there are at least three available EDPs to make a time series. Figure 2 shows the state of the EDP coverage for these 165 events. Figure 2a shows the distribution of the duration of events for all the events as estimated from the procedure above (Figure 2), which is broad with a tail at high values, median of 90 s, and minimum and maximum values of 30 and 242 s, respectively. Such durations of 1 min to several minutes are consistent with the previous report by Diéval et al. (2015). Figure 2b shows that the restrictions from the processing by Morgan et al. (2013) are such that there are not always as many EDPs available as one would wish for a complete coverage of each event. The distribution of the number of available EDPs divided by the number of ionograms during the duration of each event (i.e., ratio of numbers), for all the events, is broad with a median of 0.58 and minimum and maximum values of 0.12 and 1, respectively.

It is preferable not only to have a good proportion of EDPs available (to reduce the data gaps) but also to have the first and last available EDPs covering as close to the beginning and end (edges) of the overhead pass as possible. Figure 2c shows the distribution of the duration of the EDP coverage divided by the event duration for each event (i.e., ratio of durations), for all the events, peaking at high values, with a median of 0.85 and minimum and maximum values of 0.14 and 1, respectively; so a majority of events has available EDPs rather close to the edges of the structure, which is a good sign. Figure 2d shows a scatter plot of the ratio of durations plotted versus the ratio of numbers, colored by the number of available EDPs for the duration of each event, for all the events. Naturally, the number of available EDPs increases as both ratios increase. We decide to keep 48 events for which the number of available EDPs divided by the number of ionograms is ≥0.7 and for which the duration of the EDP coverage divided by the event duration is ≥0.7. For these 48 events we are confident that we have a reasonable EDP coverage, and therefore a reasonable determination of the shape of the time series of EDPs. The minimum and maximum values of the number of available EDPs per event become 4 and 20, respectively.

We will compare the altitude variations for the EDPs of the time series for each event, at a fixed sounding frequency, for all frequencies for which ionospheric traces were detected (the local frequency is excluded

from analysis). To make it easier to identify the shapes of density structures, we visually inspect these time series at a few selected frequencies typical for the detection of oblique echoes, to select one EDP which defines best the simplest shape of the time series, in comparison with the first and last EDPs (beginning and end edges) of the time series (i.e., using three EDPs to find the simplest shape). This selected EDP is thus a reference profile to which we compare the other EDPs in the time series, and is referred to as "point of interest" PI EDP. By choosing the PI EDP in this manner, we do not require the PI EDP to sit at the center of the time series nor at the apex of the hyperbola signature (so there can be unequal numbers of EDPs on either sides of the PI EDP). The determination of the PI EDP is somehow subjective, especially if the shape of the time series is complicated, with complex variations; in addition, the shape can change with increasing frequency, although gradually. Anyway, this exercise is made for helping identify the altitude variations relative to a reference EDP.

At a fixed frequency, the four simplest possible shapes are as follows. (1) If the altitude of the PI EDP is higher than the altitude of both beginning and end EDPs, then we call the shape "bulge." In this case, there is first an increase and then a decrease of the altitude level, the PI EDP having the highest altitude in the time series. (2) If the altitude of the PI EDP is lower than the altitude of both beginning and end EDPs, then we call the shape "dip." In this case there is first a decrease then an increase in altitude, the PI EDP having the lowest altitude in the time series. (3) If the altitude of the PI EDP is higher than the altitude of the beginning EDP and lower than the altitude of the end EDP, then we call the shape "uphill slope." (4) If the altitude of the PI EDP is lower than the altitude of the beginning EDP and higher than the altitude of the end EDP, then we call the shape "downhill slope." The PI EDP for an uphill slope or downhill slope is determined visually from the EDP bringing a change of slope along the time series; that is, this EDP can be used to test if the slope is convex or concave. The four possible simplest shapes mentioned (bulge, dip, uphill slope, and downhill slope) have been found in the 48 events we have examined, as we will see below.

In the following figures, for a given event, we either use the altitude differences between the PI EDP and all other EDPs in the time series for a detailed study, or we use the altitude differences between the PI EDP and the beginning or end EDPs (edges) for a more concise study. Several times we will work at a fixed frequency 1.936 MHz, for illustration of a typical frequency at which oblique echoes are detected. We note that the uncertainty on the range of the ionospheric echo corresponds to one pixel and is given by $c \times \Delta t/2 = 13.7$ km $= \pm 6.9$ km. For this work, it means that for an event at a fixed frequency, if the absolute value of the altitude difference between the PI EDP and another EDP of the time series is larger (smaller) than 13.7 km, then this altitude difference is resolved (unresolved) by the measurement.

3. Results

3.1. Close Look at Individual Events

In this section, we investigate the detailed variations of a few events as a function of frequency and time. Figure 3 shows time series in four columns corresponding each to one example of event with a rather clear shape in EDP time series at different frequency levels (see top row): (a) bulge, (b) downhill, (c) dip, and (d) uphill. The date and time of PI EDP for each event are indicated in the figure. In all panels, the vertical dashed lines mark particular measurement times: PI EDP (magenta), beginning and end EDPs (black), and beginning and end times determined from the echogram (green). The top row shows time series of EDPs color coded for six selected frequencies between 1.433 and 2.505 MHz. Our working frequency of 1.936 MHz lies between the green and magenta curves.

We see that bulges are indeed detected, consistent with expectations from using the uncorrected apparent altitude (e.g., Duru et al., 2006). Interestingly, other shapes are also detected: dips (as proposed by Nielsen, Wang, et al., 2007), uphill, and downhill slopes; in principle, their inclined density contour levels are able to give oblique echoes. We see sometimes complex altitude variations that tend to complicate the shape of events, but the simplest shapes were rather easy to determine for these four cases. For example, the dip event in column (c) appears more clearly as a dip if one considers the gradual decrease and then gradual increase of altitude on either side of the PI EDP, with the gradual decrease being shortly interrupted by an amplitude quirk. As we see already here, and will see again later, that the altitude variations tend to be larger at low frequency (high altitude) than at high frequency (low altitude), and the shape can remain the same at all frequencies or change with frequency.

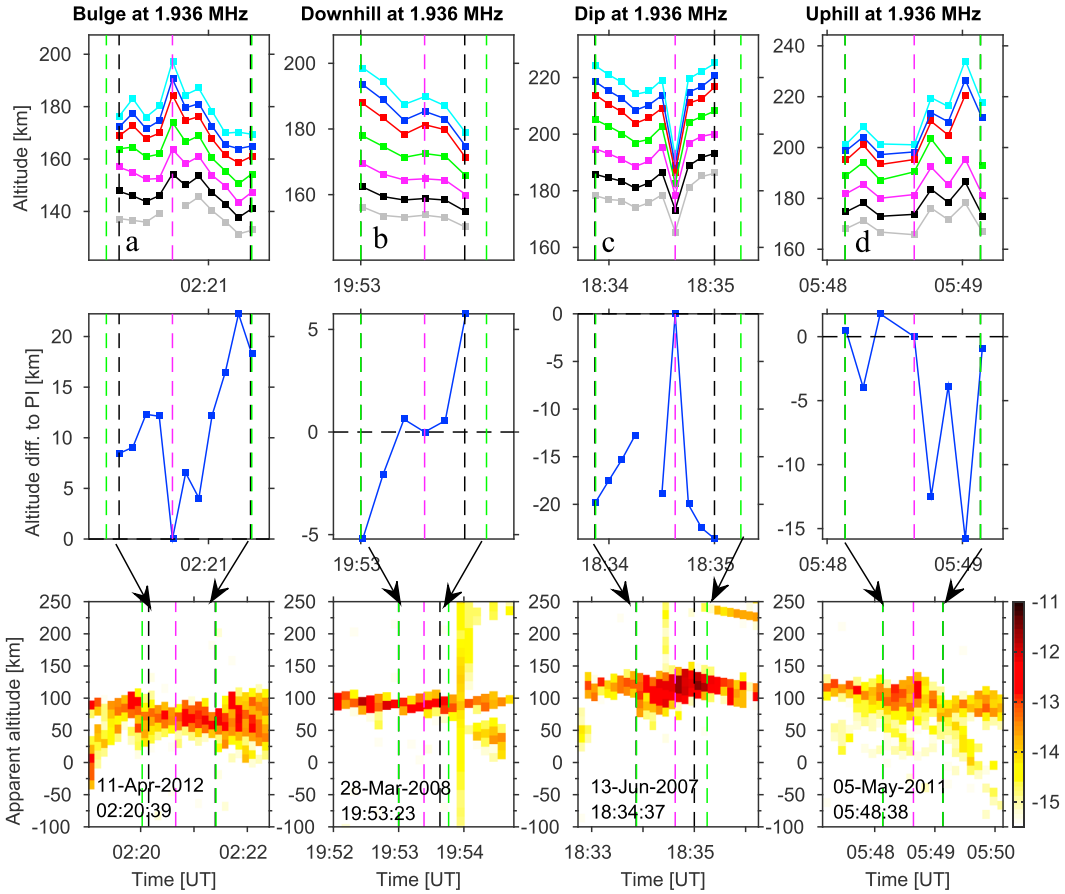

Figure 3. Examples of time series for four events. First column (a): bulge. Second column (b): downhill slope. Third column (c): dip. Fourth column (d): uphill slope. In all panels, the green vertical dashed lines mark the times selected for the beginning and end edges of the hyperbola signature; the black vertical dashed lines mark the times of the first and last available EDPs for the structure; the magenta vertical dashed line marks the time of PI EDP. First row: time series of available EDPs at different frequencies coded by color: 1.433 (cyan), 1.542 (blue), 1.651 (red), 1.848 (green), 2.067 (magenta), 2.286 (black), and 2.505 (grey) MHz, corresponding to 2.55×10^4, 2.95×10^4, 3.38×10^4, 4.23×10^4, 5.3×10^4, 6.48×10^4, and 7.78×10^4 cm^{-3}. The filled squares mark the measurement values of altitudes. Second row: time series of altitude difference between the PI EDP and each EDP, for the frequency level 1.936 MHz; values are zero for the PI EDP and for EDPs of identical altitude, positive for EDPs standing lower than the PI EDP, and negative for EDPs standing higher than the PI EDP. The horizontal black dashed line marks altitude difference = 0. Third row: echograms integrated between 1.8–2 MHz, in the same format as in Figure 1. Notice the longer time scale shown, indicated by arrows. The date and time for the PI EDP of each event are indicated in the bottom row.

The second row of Figure 3 shows the time series of altitude differences between the PI EDP and the other EDPs of the time series for these four events, at a fixed frequency 1.936 MHz. Positive values mean that the PI EDP stands at higher altitude than these EDPs, negative values mean that the PI EDP stands at lower altitude than these EDPs, and zero values correspond to the PI EDP or any EDP with identical altitude. For clarity, the magenta vertical dashed line indicates the position of the PI EDP. At frequency 1.936 MHz, there are 33 events out of 48 classified as bulges, 6 as dips, 4 as downhill slopes, 3 as uphill slopes, and 2 undetermined (data gap). As we will see later, at this frequency, the bulges dominate the number of events, compared to other shapes. Interestingly, this result, based on altitude profiles corrected for dispersion, confirms the insights of Gurnett et al. (2005) and Duru et al. (2006) based on the apparent altitudes uncorrected for dispersion.

In the bottom row of Figure 3, we inspect the hyperbola signatures in the echograms integrated for 1.8–2 MHz for these four events. These panels have an extended time range to give a better view of the oblique echoes caused by the density structures. While the hyperbola signature in column (a) presents two clear legs (here there is a bulge), the hyperbola signature in the other columns have only one clear leg, with the leg at the beginning of the signature for column (c) (here there is a dip) or the leg at the end of the signature for columns (b) and (d) (here there are downhill and uphill slopes, respectively). We also see that

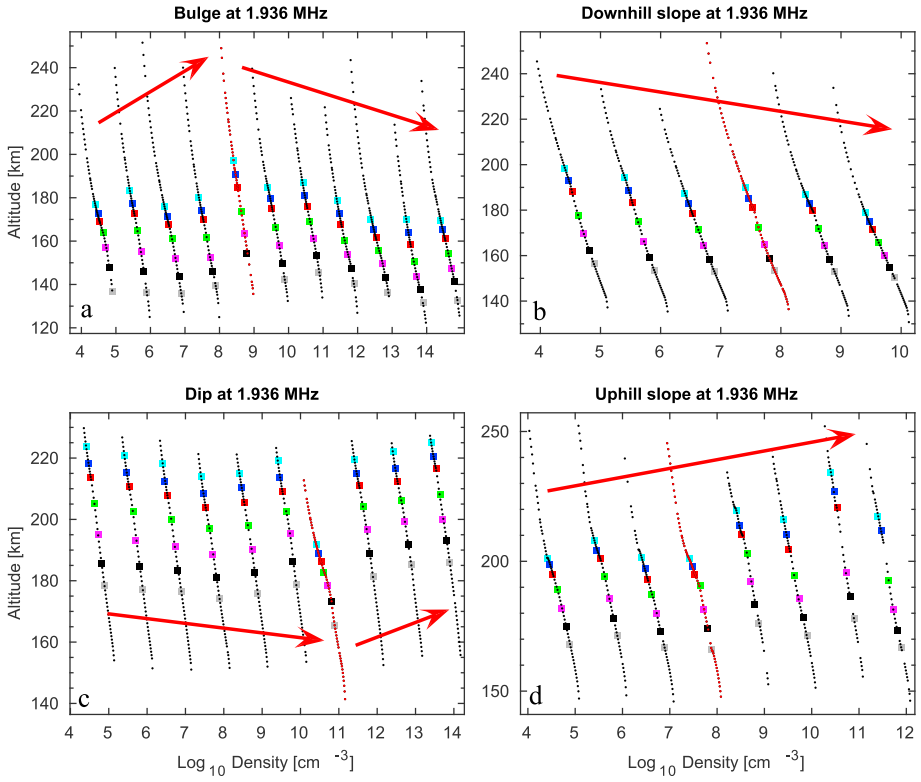

Figure 4. Series of EDPs for the same Four events: (a) bulge, (b) downhill slope, (c) dip, and (d) uphill slope. In each panel, the red curve is the PI EDP; the black curves are the other EDPs for the time series. The local frequency was excluded from analysis; the colored squares represent the same data points as in Figure 3 (same color coding for frequency). For each event, the EDPs are shown versus $\log_{10}$(density) in cm^{-3}, and the densities of the successive EDPs are multiplied by 10^0, 10^1, 10^2, etc., for clarity. The red arrows are added to guide the eye.

the point of highest apparent altitude on the hyperbola signature does not necessarily correspond to the highest (or even lowest) altitude point (for bulges and dips) in the time series of corrected altitudes from the top row. Examination of the other events in the list suggests two points. (1) The variations of the apparent altitude of the hyperbola signature on the echogram bear no predictable relation to the variations of the corrected altitudes in the same frequency range. (2) The presence of two clear hyperbola legs or only one clear leg at the beginning or end of the structure cannot be reliably related to the simplest shape of structures in the same frequency range. One could have expected, from considerations of spacecraft motion moving toward and then away from a structure, that the slopes on either side of a bulge or dip should cause two clear legs at the beginning and end of the structure, while an uphill slope would cause just one clear leg at the beginning of the structure and a downhill slope would cause just one clear leg at the end of the structure. It is likely that the key to understand these two issues arises from both the signal dispersion (including varying group velocity and raypath bending as the plasma frequency of the medium changes during their propagation) and the likely complicated geometry of the raypaths related to the presence of horizontal density gradients (possible multiple reflections for a given ray). Ray tracing through models of ionospheric layers obtained from the MARSIS measurements, taking signal dispersion into account, would be illuminating to solve these two issues, although it is beyond the scope of the present work.

In Figure 4 we check the EDPs for their full frequency range for the same four events. Figure 4 displays the series of EDPs for each event into four panels: bulge (a), downhill slope (b), dip (c), and uphill slope (d). For each event, the red curve is the PI EDP, the black curves are the other EDPs for the time series, and the colored dots mark the same data points (color coded with frequency) as in Figure 3. For each event, the EDPs are plotted versus $\log_{10}$(density) in cm^{-3} and the densities of the successive EDPs are multiplied by 10^0, 10^1, 10^2, etc., for clarity. Because this way of displaying EDPs is equivalent to a time series of EDPs, one can see that for each event, the shapes of the color coded altitude variations at the various frequencies follow the

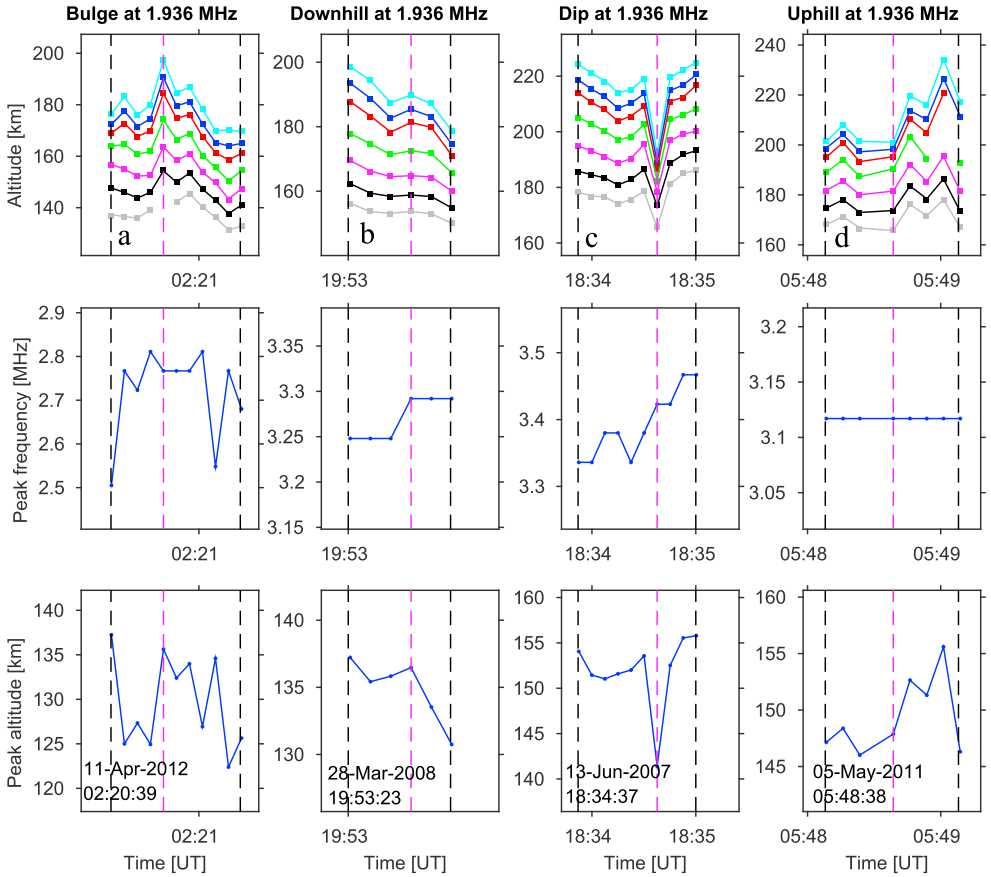

Figure 5. Examples of time series for the same four events. First column (a): bulge. Second column (b): downhill slope. Third column (c): dip. Fourth column (d): uphill slope. First row: almost same format as first row of Figure 3. Second row: time series of peak frequency. Third row: time series of peak altitude.

same shapes as in Figure 3. We remark for these four events (noticed also for the other events in the list) that the altitude range of these EDPs actually shifts down or up in altitude to follow the shape in the time series of EDPs from Figure 3; the ionospheric peak altitude tends to follow this trend too. For example, for the bulge event, the altitude range of each EDP shifts upward until the PI EDP is reached, then the altitude range of the following EDPs shifts down, like the entire topside ionosphere moves up then down in altitude. Similarly, the entire topside ionosphere appears to continuously move up for the uphill event, continuously move down for the downhill event and first move down then move up for the dip event. We note that the absolute value of the difference in SZA between the first and last EDPs of the time series for each event is typically small, with a median of 1.6°; thus, these altitude changes are independent of the SZA.

When examining the EDPs for the overall of events of the list, there are sometimes hints of vertical gradients in the form of slight ledges, for example, at 220 km altitude for the fifth EDP from the left in panel (d). These vertical gradients may be density bite-outs, density bumps, and topside layers (e.g., Kopf et al., 2008; Withers et al., 2005), which would have been attenuated in the EDPs because of two reasons. (1) When there is a nonmonotonic variation in the electron density (i.e., a valley: decrease in density as altitude decreases above the main peak), MARSIS cannot observe this valley directly because low-frequency signals get reflected at layers of larger plasma frequency present at higher altitudes above the valley, although indirect observations are possible (e.g., Wang et al., 2009). (2) The processing of the EDPs by Morgan et al. (2013) assumes monotonic profiles.

We examine the trends of ionospheric peak altitude and peak frequency for the same four events in Figure 5, which is organized as columns: (a) bulge, (b) downhill slope, (c) dip, (d) uphill slope. The first row has almost the same format as the first row of Figure 3. The second and the third rows show time series of peak frequency and peak altitude, respectively. For these events, the variation of the peak frequency presents

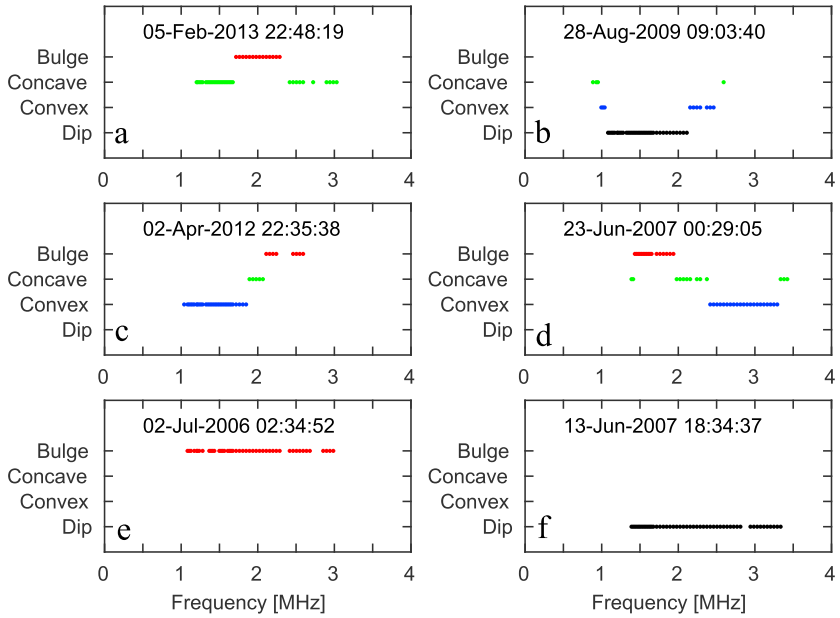

Figure 6. (a–f) Examples of classification of the simplest shape of events as a function of frequency, for six events (date and time of PI EDP are indicated in each panel). The vertical axis displays the shape with corresponding colored dots: bulge (red), concave slope (green), convex slope (blue), and dip (black). The local frequency was excluded from analysis.

no clear relationship compared to the variation of the altitude levels at a few lower frequencies: although the peak frequency tends to increase during the bulge event, the peak frequency just increases during the downhill slope event, also just increases during the dip event and stays constant during the uphill event. From looking at the rest of the events in the list, there is no systematic increase (or decrease) in peak density in the regions giving oblique echoes. We note that individual cases of high peak densities in areas of strong near-vertical crustal fields were reported by, for example, Nielsen, Fraenz, et al. (2007). On the other end, the evolution of the peak altitude for the four events tends to follow the variations of altitude levels at lower frequencies, such as to track the shape of the time series of EDPs. This trend was observed as well for the rest of the events in the list.

Finally, the evolution of the simplest shape of events with frequency is also examined for the full frequency range of a few selected events. Figure 6 shows the shape classification of six events as function of frequency, displayed as colored dots: bulge (red), concave slope (green), convex slope (blue), and dip (black). Here we use the altitude differences between the PI EDP and the first or last EDP of the time series, at a fixed frequency, for every frequency of each event. It is useful to consider the convex or concave nature of a slope here, because a convex slope swells downward (looks like a dip) and a concave slope swells upward (looks like a bulge). For a given slope event, at a fixed frequency, the event is determined as convex (concave) if the second derivative of the altitude from the time series of three EDPs is positive (negative). The date and time of the PI EDPs are indicated in each panel. In Figures 6e and 6f, the event remains with the same shape at all frequencies: bulge and dip, respectively. In Figure 6a, the event evolves from concave, to bulge then to concave, as frequency increases. In Figure 6c, the event evolves from convex, to concave, then to bulge. In Figure 6b, the event evolves from concave, to convex, to dip, to convex, and then to concave. In Figure 6d, the event evolves from concave, to bulge, to concave, to convex, and then to concave.

It is observed that the shape change is gradual such that there are always concave and convex slopes in the correct order to separate bulges and dips; this is natural since a concave slope looks like a bulge and a convex slope looks like a dip. This is confirmed by examining the other events in the list. We see that in the case of events changing shape over frequency, if the shape is not a bulge in a given segment of the frequency range, there is no marked preference for observing dips rather than convex slopes or concave slopes. This holds for the entire frequency range. Note that the shape of an individual event at a fixed frequency may be uncertain if the altitude differences are unresolved, that is, in absolute value are lower, than the 13.7 km range

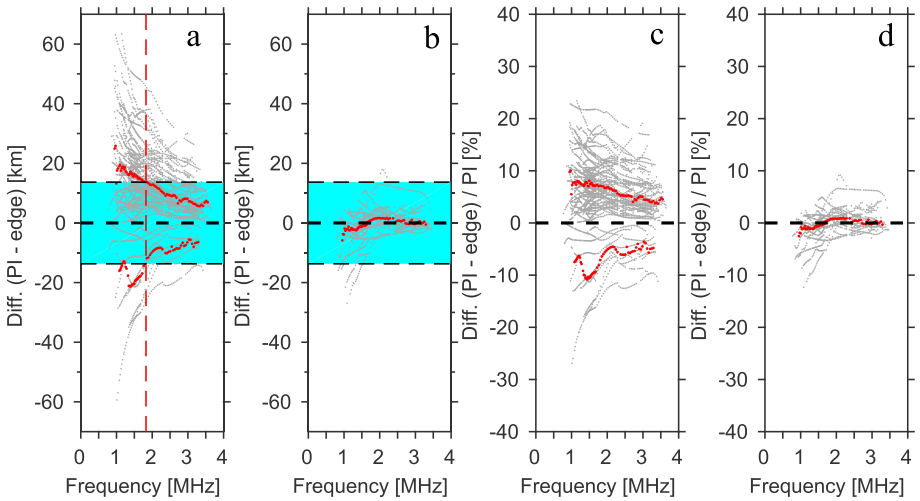

Figure 7. (a and b) Altitude differences PI EDP-edge EDP (in km) for all the events as a function of frequency, plotted as grey lines. (c and d) Altitude differences PI EDP-edge EDP relative to the altitude of the PI EDP (%) for all the events as a function of frequency, plotted as grey lines. The edge EDP refers to either the first EDP or the last EDP of the time series of each event. Altitude differences which change sign over frequency are plotted in columns (b and d), while altitude differences which keep either all-positive or all-negative over frequency are plotted in columns (a and c). The local frequency was excluded from analysis. The red dots indicate the median of the altitude differences as a function of frequency. In panels (a) and (c), the medians are shown separately for the all-positive and the all-negative altitude differences. In panels (a) and (b), the thin horizontal black dashed lines mark the 13.7 km and −13.7 km thresholds, and the regions with abs(altitude difference) $<$ 13.7 km are colored in cyan, and the regions with abs(altitude difference) $>$ 13.7 km are left in white, to help with clarity. In panel (a), the vertical red dashed line marks the threshold frequency 1.826 MHz (see text).

resolution (this is the case for many events as we will see later). Despite this, there is a systematic gradual transition over frequency. This result validates the determination of shape over frequency for individual events, whatever the magnitude of the altitude differences.

3.2. Statistics

Now we consider all the events for statistics purposes. We start with inspecting the magnitude of the altitude differences for all the events as a function of frequency for the entire frequency range. Figures 7a and 7b show the altitude differences between the PI EDP and the edge EDP of each event, versus frequency, for all the events, and similarly, in Figures 7c and 7d, the altitude differences between the PI EDP and the edge EDP relative to the altitude of the PI EDP of each event. The edge EDP is either the first or last EDP of the time series of a given event. Altitude differences that change sign over frequency are plotted in Figures 7b and 7d, while altitude differences keeping the same sign over frequency are plotted in Figures 7a and 7c. Median values of the altitude differences over frequency are indicated by red dots. The median values of the altitude differences being all positive or all negative over frequency are treated separately. The horizontal black dashed lines delimitate regions where the absolute values of altitude differences are less than or greater than 13.7 km (13.7 km is the range resolution). The colored patches in Figures 7a and 7b help distinguishing these regions of resolved or unresolved altitude differences (cyan or white).

In Figures 7a and 7c, the altitude differences tend to be larger in absolute value at low frequency than at high frequency, both for all-negative and all-positive differences. These trends are also reproduced by the medians values. The largest values of altitude differences (several tens of kilometers or several tens of % relative to the PI EDP) are found at low frequencies, and the lowest values (several kilometers or several % relative to the PI EDP) at high frequencies. Thus, it is more likely for the altitude differences to be unresolved ($<$13.7 km) at high frequencies (low altitudes) than at low frequencies (high altitudes). The absolute value of the median of altitude differences becomes larger than 13.7 km at a fixed frequency of 1.848 MHz (1.805 MHz) for the all-negative (all-positive) altitude differences. Finally, a majority of altitude differences lie completely within the unresolved region (cyan patch). Similarly, for the altitude differences changing sign over frequency (Figures 7b and 7d), the altitude differences tend to be larger in absolute value at low frequency than at high frequency. These trends are also reproduced by the medians values. The contribution of both negative and positive values at each frequency contributes to decrease the absolute value of the median, to be below

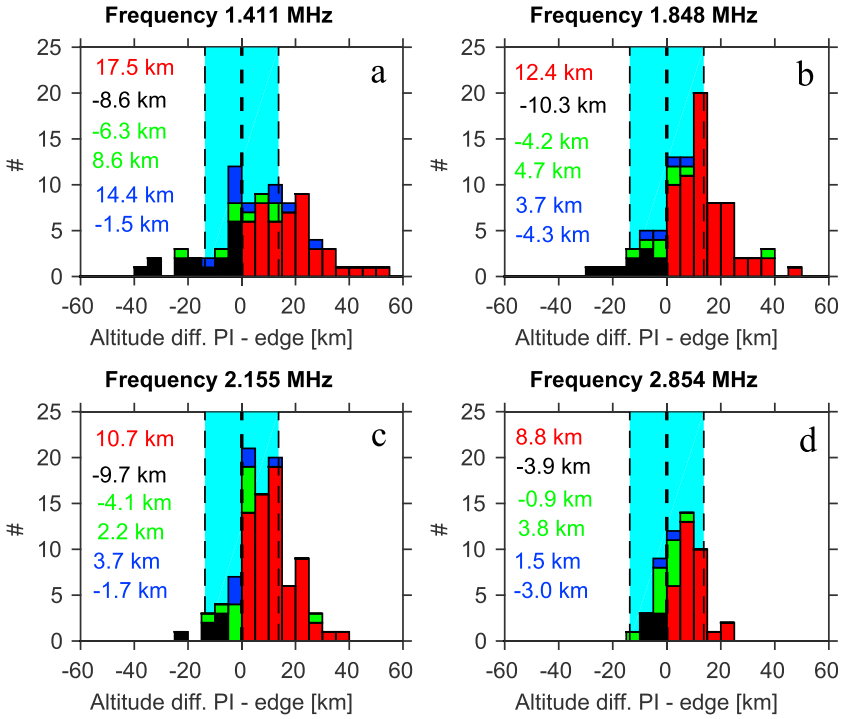

Figure 8. Distributions of altitude differences PI EDP-edge EDP of each event, for all the events, at four fixed frequencies: (a) 1.411, (b) 1.848, (c) 2.155, and (d) 2.854 MHz. The edge EDP is either the first or last EDP of the time series of an event. In each panel, the total distribution is separated into stacked color coded distributions for the four simplest shapes (same color code as Figure 6): bulge (red), dip (black), uphill slope (blue), and downhill slope (green). This means that in each bin, we count the number of events for each of the four event shapes and then trace colored bars stacked on top of each other; each bar corresponds to one event shape, and its length is equal to the number of events. The thin vertical dashed black lines delimitate the regions of abs(altitude differences) $<$ or $>$ 13.7 km, with corresponding colored patches (cyan or white) for clarity. The median values of altitude differences for the different distributions are indicated in the panels with the same color code per type of shape.

13.7 km. The results are consistent with the finding by Nielsen, Wang, et al. (2007) of density contours being more tilted at low frequencies than at high frequencies.

In Figure 8, we check the distributions of altitude differences between the PI EDP and the edge EDP, for all the events, separated between the four simplest shapes, at four different frequencies corresponding to four panels: (a) 1.411, (b) 1.848, (c) 2.155, and (d) 2.854 MHz. In each panel, the distributions are color coded per shape and plotted as stacked bars on top of each other in every bin: bulge (red), black (dip), downhill slope (green), and uphill slope (blue). Regions of abs(altitude differences) $<$ or $>$ 13.7 km are delimited by thin vertical black dashed lines and colored patches (unresolved: cyan, resolved: white). For bulges, both sides of the structure has positive values of altitude differences; similarly, for dips, both sides have negative values of altitude differences; for uphill slopes the value of altitude difference is positive for the first EDP and negative for the last EDP; for downhill slopes the value of altitude difference is negative for the first EDP and positive for the last EDP. At the four frequencies shown, the number of bulges dominates the number of other shapes (we will see this also later). As frequency increases, the spread of altitude difference values tends to decrease for each shape, with less extreme values present, such that the distributions become more confined within the region of abs(altitude differences) $<$ 13.7 km (cyan). At a fixed frequency, the absolute value of the altitude differences tends to be larger for bulges than for other shapes and tends to be larger at low frequency than at high frequency for bulges but less evident for other shapes (see also the median values for the four distributions of simplest shapes indicated as color coded text in each panel). There may be an effect of the number of events regarding the trends of bulges versus other shapes, since there are far more bulges than other shapes, as we will see later. For illustration, the median value of 12.4 km for the altitude differences in bulges at a fixed frequency 1.848 MHz is of the same order as the rms apparent altitude difference between the hyperbola apex and the main ionosphere of 19 km at a fixed frequency 1.8 MHz determined by Duru et al. (2006).

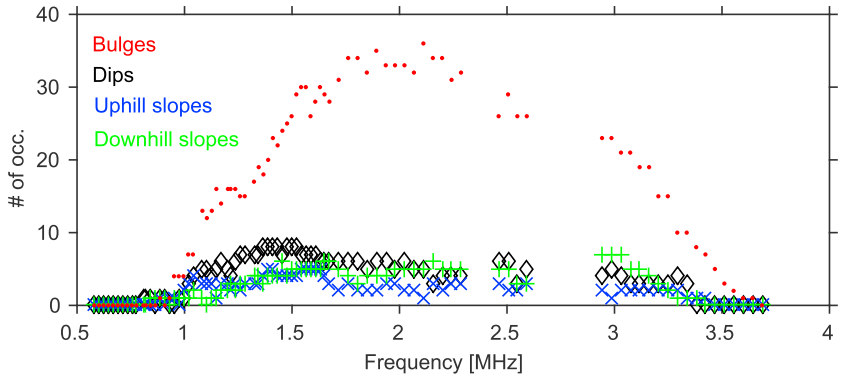

Figure 9. Distribution of the four simplest shapes as a function of frequency, for all the events, displayed as colored symbols, with the same color code as Figures 6 and 8: bulges (red dots), dips (black diamonds), uphill slopes (blue crosses), and downhill slopes (green plus signs). Data points at frequency levels within in the sensitivity gaps are not displayed to avoid a bias.

We also examine, in Figure 9, the distribution of the four simplest shapes of all events in the entire frequency range, displayed as color coded symbols: bulges (red dots), dips (black diamonds), downhill slopes (green "plus signs"), and uphill slopes (blue "crosses"). The number of events drops sharply at frequencies below 1 MHz because of the various issues of signal-to-noise ratio mentioned earlier and drops sharply at frequencies above 3 MHz (1.1×10^5 cm^{-3}) because the ionospheric echo is constrained by the peak density (which varies between 0.5 and 1.5×10^5 cm^{-3} on dayside; see, e.g., Morgan et al., 2008). The distribution of bulges dominates the total number of events and peaks at 2.111 MHz with 36 events; at the same frequency there are five downhill slope events, one uphill slope event, and five dips. The distribution of uphill slope events peaks with five events at seven different frequencies—those highest is 1.63 MHz; for downhill slope events it peaks with seven events at three frequencies—those highest is 1.455 MHz, and for dips it peaks with eight events at seven different frequencies—those highest is 1.52 MHz. Thus, the number of bulges peaks at a much higher frequency than the numbers of other shapes does. For frequencies below 0.951 MHz all shapes have comparably small numbers of events. This is likely an effect of bad statistics, since there are challenges for measuring the ionospheric trace at frequencies <1 MHz. For higher frequencies the number of bulges is much larger than the other numbers. It is worthwhile to note that for the 48 events, there are 20 events detected during MEX passes going from North to South, and 28 events detected during passes going from South to North; still the proportions of uphill and downhill slope events remain similar in both instances, as expected.

Finally, we can compare the behaviors of the ionospheric peak altitudes and peak frequencies to the behavior of the altitude level at 1.936 MHz, for all the events, to check the case studies trends from Figure 5. Then, Figure 10 shows scatter plots of the altitude level at 1.936 MHz versus the peak frequency (Figure 10a) and versus the peak altitude (Figure 10b), both using all the available EDPs in the time series of all the events. As suggested from the inspection of individual events, we see that when the selected altitude level increases, the peak frequency has a weak trend of increase (broad scatter), while the peak altitude has a clear trend of increase (narrow scatter). We confirm that these trends remain visible (especially for the peak altitude) when

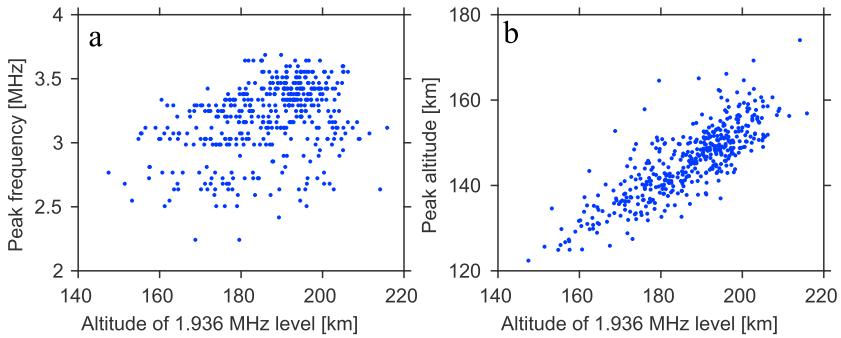

Figure 10. Scatter plot of the altitude level at a fixed frequency 1.936 MHz versus the (a) ionospheric peak frequency and versus the (b) ionospheric peak altitude.

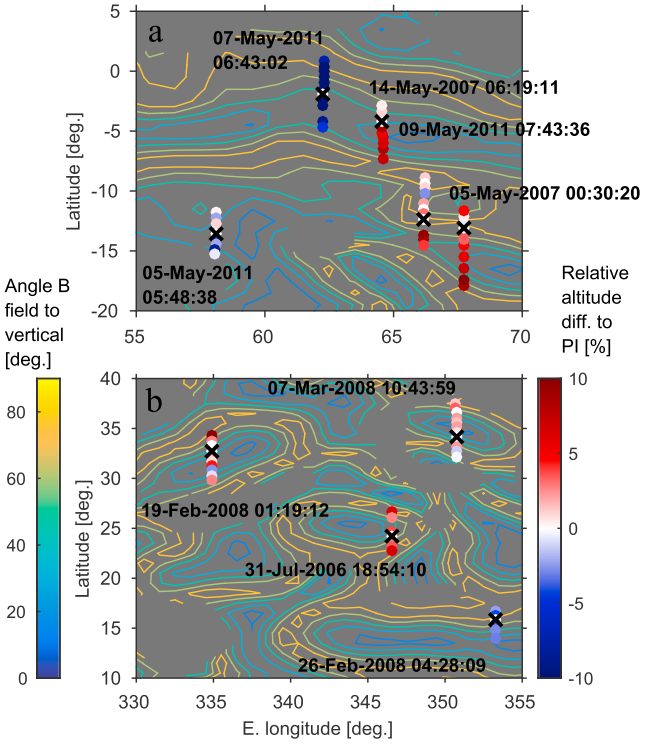

Figure 11. Maps showing regions of moderate crustal field strengths near the equator, in the (a) southern hemisphere and (b) northern hemisphere. These are maps of the angle of the crustal magnetic field to the vertical from the model of Cain et al. (2003) evaluated at 150 km altitude, represented as color coded contours from 15 to 75° per step of 15° (going from near horizontal to near vertical), using the colorbar on the left side. Fields of strength <30 nT are ignored. The footprint of MEX at the times of available EDPs of the time series of the individual events observed in these regions are superposed onto the maps, colored for each event by the altitude differences between the PI EDP and the other EDPs relative to the altitude of the PI EDP (in %), all taken at a fixed frequency 1.936 MHz. Negative altitude differences are colored in blue, zero differences in white, and positive differences in red, using the colorbar on the right side. The date and time of the PI EDP are written next to each event, and its location marked by a black cross.

separating the events into the four types of simplest shapes at 1.936 MHz (not shown). For the case of bulges (the majority of events), the peak altitude has a marked tendency of a local increase and the peak frequency has a less evident tendency of a local increase, in areas of oblique echoes.

3.3. Influence of Crustal Magnetic Field Orientation

Previous studies have shown the close association between oblique echoes and near-vertical crustal magnetic fields (e.g., Gurnett et al., 2005). Here we inspect the relationships of the altitude differences in areas of oblique echoes and corresponding magnetic anomalies, first for a few individual events, then for all the events. We use the Cain et al. (2003) crustal magnetic field model evaluated at 150 km altitude at MEX footprint.

Figure 11 shows maps of two regions of magnetic anomalies of moderate strength near the equator, in the southern hemisphere (Figure 11a) and northern hemisphere (Figure 11b). Selected contours of the angle of the crustal magnetic field to the vertical are displayed using the left side colormap. The horizontal orientation is 0°, and the vertical orientation is 90°. Field strengths <30 nT are ignored. The footprints of MEX location at the times of available EDPs for individual events detected in these regions are superposed onto the maps. The location of the PI EDP is marked by a black cross for each event and its date and time written in the panels. The events are each colored with the altitude differences between the PI EDP and the other EDPs of the time series relative to the altitude of the PI EDP (in %), all taken at a fixed frequency 1.936 MHz. Negative values mean that the PI EDP stands at altitudes below these EDPs, zero values mean that the PI EDP stands at the same altitude as these EDPs (the PI EDP itself or other EDPs of equal altitude), and positive values mean that the PI EDP stands at altitudes above these EDPs. Negative values are in blue, zero values in white, and positive values in red, using the colormap on the right side.

In both maps, there are events detected geographically close to each other, at different dates and times, with similar shapes or different shapes, from their altitude differences. Thus, the shape may vary in geographical location and time. The range of crustal field orientations, through the latitudinal extension of the events (MEX orbits are nearly fixed in longitude near the equator), covers well the areas of near-radial field near the center of the events and the areas of near-horizontal field near their edges. The time of the PI EDP is determined from the time series of EDPs and is not necessarily associated to near-vertical fields.

Finally, we check whether the magnitude and the sign of the altitude variations at a fixed frequency 1.936 MHz are affected by the crustal field orientation, for all the available EDPs of the time series of all the events, in Figure 12. The data points of the altitude differences between the PI EDP and itself (which are zero values) are removed from this figure, so the zero values which remain are only due to other EDPs with altitudes identical to the PI EDP. Figure 12a displays the distribution of the angle of the crustal field to the vertical, which covers the full range of possible angles (minimum and maximum are 2.5 and 89.5°), with 25th, 50th, and 75th percentiles of 26.6, 42.0, and 61.8°, respectively. The distribution peaks at angles closer to the vertical than to the horizontal (it peaks at angles <45°). This is expected because the density structures giving oblique echoes are usually found in areas of vertical to oblique crustal field orientation, with a latitude extension covering the latitude extension of the magnetic cusps, the magnetic field strength being not important (e.g., Diéval et al., 2015; Duru et al., 2006). The time series of EDPs cover whenever possible up to the edges of the density structures as determined from the echograms; thus, angles closer to the horizontal are also sampled, particularly near the edges.

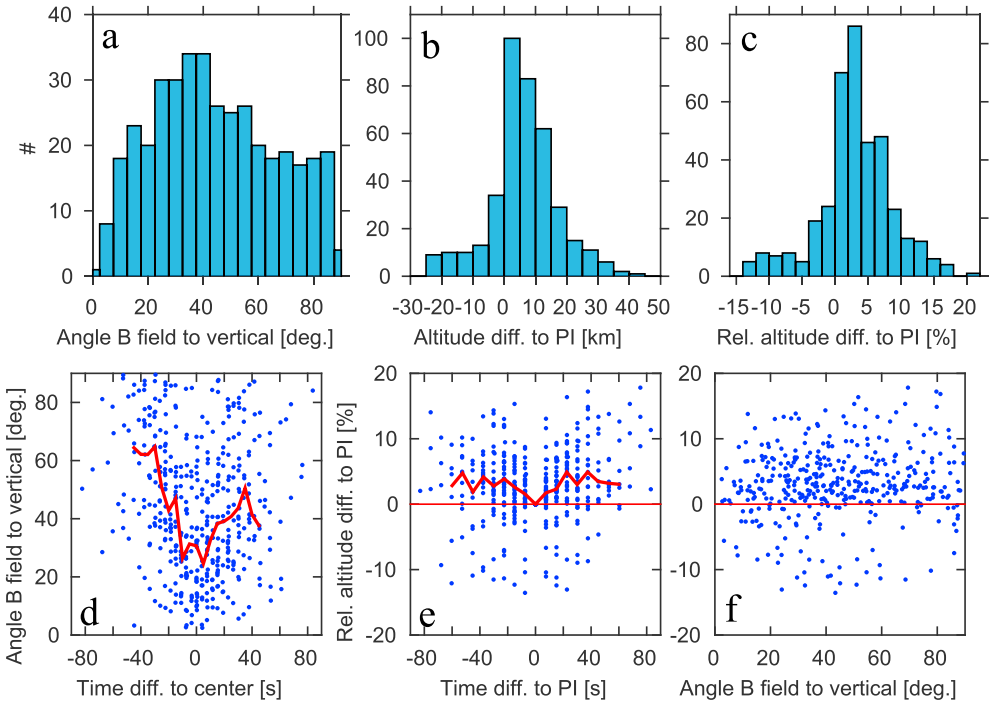

Figure 12. In this figure, the data points correspond to the altitude level at a fixed frequency 1.936 MHz of all the available EDPs of the time series of all the events. (a) Distribution of the angle of the crustal magnetic field to the vertical. (b) Distribution of the altitude differences between the PI EDP and the other EDPs of the time series per event. (c) Distribution of the altitude differences between the PI EDP and the other EDPs of the time series, relative to the altitude of the PI EDP (in %), per event. (d) Superposed epoch analysis of the angle of the crustal field to the vertical, using the time difference in seconds compared to the center time of the density structure (which is centered at 0 s). Negative times are before the center time and positive times are after. The red line indicates the median values as a function of superposed epoch time. (e) Superposed epoch analysis of the relative altitude differences, using the time difference in seconds compared to the PI EDP time (which is centered at 0 s). Negative times are before the PI EDP time, and positive times are after. The red line indicates the median values as a function of superposed epoch time. (f) Scatter plot of the angle of the crustal field to the vertical versus the relative altitude differences.

Figure 12b shows the distribution of the altitude differences between the PI EDP and the other EDPs of the time series, which presents negative and positive values (minimum and maximum are −24.7 and 44.1 km), peaks at positive values (there is a majority of bulges which contribute positive altitude differences), with 25th, 50th, and 75th percentiles of 1.1, 5.8, and 12.3 km, respectively. There are 390 data points, whose 309 are positive differences and 76 are negative ones. In absolute value, typically, the smallest altitude differences are found close to the PI EDP, and the largest values close to the edges of the structure. Figure 12c shows the distribution of altitude differences between the PI EDP and the other EDPs of the time series, relative to the altitude of the PI EDP (in %), which shows similar behavior to the former distribution. It presents negative and positive values (−13.5 and 21.2%, respectively), peaks at positive values, with 25th, 50th, and 75th percentiles of 0.6, 2.9, and 6.4%, respectively.

Figure 12d displays a superposed epoch analysis of the angle of the crustal field to the vertical, using the time difference in seconds between the available EDP in the time series and the center time of the density structure (positive values are after and negative values are before the center time, respectively). For each event, the center time is the time at the center of the interval bounded by the edges of the structure as determined from the echogram. A red line indicates the median values of angles as a function of superposed epoch time. The distribution varies like a broad "v" shape, as well as the median values. We have checked that individual time series often vary such as to be centered near a "v" shape. The crustal field orientation changes from more vertical to more horizontal, as one progress from the center of the structures toward their beginning and end edges. This trend is expected, since the latitudinal extension of the structures giving oblique echoes tends to cover the latitudinal extension of the corresponding magnetic cusps (e.g., Diéval et al., 2015).

Figure 12e displays a superposed epoch analysis of the relative altitude differences, using the time difference in seconds between the available EDP in the time series and the PI EDP (positive values are after and negative values are before the PI EDP, respectively). A red line indicates the median of the relative altitude differences

as a function of superposed epoch time. When considering the majority of points being positive, the distribution varies like a broad "v" shape. We have checked that individual profiles plotted in this way do not necessarily exhibit a clear "v" shape (even when including only bulges), because of the ample fluctuations existing in the time series. The median values also vary as a "v" shape. Since the majority of density structures are bulges, this means that the altitude level at a fixed frequency tends to stand further down (relative to the PI EDP) as one progresses toward both beginning and end edges of the structures.

Figure 12f shows a scatter plot of the angle of the crustal field angle to the vertical versus the relative altitude differences. There is no obvious trend here, with an extended range of altitude differences (both for positive and negative ones) whatever the crustal field orientation. Considering the events of the four simplest shapes separately does not affect this result (not shown). There is, however, a slight trend to find the largest positive values toward large angles, that is, to find the edges of the density structures (mostly bulges) near the edges of magnetic cusps (near-horizontal field orientation).

4. Discussion

We have examined the behavior of the density structures from the lowest measurable densities down to the densities approaching the ionospheric peak. The absolute value of the median of altitude differences becomes larger than 13.7 km at a fixed frequency of 1.848 MHz (1.805 MHz) for the all-negative (all-positive) altitude differences between the PI EDP and the edge EDPs; we take the typical transition frequency as the average between these two values: 1.826 MHz, corresponding to 4.13×10^4 cm^{-3}. This threshold is marked with a vertical red dashed line in Figure 7a.

It is important to note that the ionosphere has several regimes depending on altitude. At low altitude near the ionospheric peak (near 125 km altitude at SZA = 0°) the plasma is in photochemical equilibrium (electron production rate balances recombination); for ions the transport time is much longer than the chemical loss time. At high altitude the chemical loss time becomes much longer than the transport time because of the reduced densities; the ions are then transported over significant distances before they are lost to chemical reactions: the ionosphere is in the transport regime (above 200 km altitude). We can check the altitude range for the behavior of the density structures and compare it to these regimes. For this purpose, we use the empirical model of the Martian dayside ionosphere by Němec, Morgan, Gurnett, Duru, and Truhlík (2011) and Němec, Morgan, Gurnett, and Andrews, (2016), based on MARSIS AIS EDPs, which incorporates dependencies on the solar radio flux F10.7, the Sun-Mars distance R, and the strength of the crustal magnetic field B at 400 km altitude (see http://aurora.troja.mff.cuni.cz/nemec/n11/). We take average conditions since the list of events covers different periods over several Martian years, and we use conditions of moderate magnetic anomalies: F10.7 = 90 solar flux units, R = 1.5 AU, and B = 30 nT.

The altitude of the level 4.13×10^4 cm^{-3} (1.826 MHz) varies from 198 km at SZA = 0° to 188 km at SZA = 85°. Therefore, there is a transition altitude of ~ 190–200 km on dayside; below (above) this altitude, the altitude differences tend in absolute value to be lower (higher) than 13.7 km. Above this altitude range, transport processes are dominant, while below this altitude range, chemical reactions are dominant. In Figure 1, we have illustrated the effect of increasing frequency on the visibility of the hyperbola signatures. For example, at 1.52 MHz (Figure 1b) the signatures are all well pronounced, while at 3.03 MHz (Figure 1e) they become smaller. The altitude of the level for 1.52 MHz (2.86×10^4 cm^{-3}) varies from 217 km at SZA = 0° to 207 km at SZA = 85°; this altitude range of 207–217 km is found within the transport dominated region. The altitude of the level for 3.03 MHz (1.14×10^5 cm^{-3}) reaches 153 km at SZA = 0°; this altitude level is found at altitudes where photochemistry prevails. Bulges are the most commonly observed structure in the topside ionosphere, present within the transport region with large-altitude differences and present within the photochemical region with small altitude differences.

These large and often positive altitude differences PI EDP-edge EDP (>13.7 km) at altitude above ~200 km can be related to upward diffusion along vertical crustal magnetic field lines, in the altitude range of transport regime. This idea was proposed by Matta et al. (2015), who successfully modeled the formation of density bulges in areas of near-radial crustal fields, using a 2-D ionospheric model incorporating field-aligned transport. Matta et al. (2015) found that the altitude difference between the density structure and the surrounding normal ionosphere increases when the altitude increases, starting from ~170 km altitude, that is, at altitudes

where transport becomes important. On the other hand, Matta et al. (2015) did not predict the formation of bulges at altitudes below ~170 km, where they found the ionosphere to have a photochemical behavior, without any vertical transport effects. In contrast, our observations show the presence of density structures at altitudes below ~200 km, with smaller altitude differences ($<$13.7 km) becoming increasingly small as altitude decreases. In addition, the entire topside ionosphere seems to move up and down, including the ionospheric peak, in the areas giving oblique echoes. In these areas, the peak densities did not change predictably. Therefore, we need an additional mechanism that may explain these observations in the altitude range of photochemical equilibrium. Such mechanism may be as follows.

Previous observations of the Martian dayside ionosphere during periods of global dust storms indicate that the peak altitude and the top of the ionosphere both rise in altitude, while the peak density does not change much (e.g., Hantsch & Bauer, 1990; Wang & Nielsen, 2003; Withers et al., 2015). The top of the ionosphere as defined by Withers et al. (2015) is "the altitude above the peak at which electron densities first fall below 1500 cm^{-3} when moving upward in altitude". These behaviors are interestingly similar to our observations in areas of oblique echoes. The mechanism for the dust storm effects has been described by, for example, Wang and Nielsen (2003) and references therein. During a global dust storm, the lower atmosphere becomes dusty, and this dust load increases the energy absorption from the Sun, which increases the neutral temperature of the lower atmosphere. The heated atmosphere then expands and gets redistributed vertically, such that the neutral density increases in the thermosphere. Maxima in the neutral density of the upper atmosphere correspond to maxima in the peak altitude. Withers et al. (2015) found that both the top of the ionosphere and the peak altitude move up and then down in altitude (by a few tens of kilometers for the top of the ionosphere and a few kilometers for the peak altitude), as the global dust storms grow and then decay. In analogy, we think there is a possible heating source (which we discuss later on), localized in areas of near-vertical crustal fields, which may locally alter the vertical distribution of the ionizable neutral atmosphere and cause subsequent raises of the altitude of the density profiles (without affecting the peak densities), such as we observe in the series of altitude profiles. Both mechanisms mentioned earlier (neutral atmosphere expansion and ionospheric plasma diffusion) may then simultaneously operate in the regions of near-vertical fields, such as to produce density structures in the entire altitude range of the topside ionosphere.

The density structures reoccur in the same areas of magnetic anomalies on the dayside (Andrews et al., 2014), no matter the field lines being closed or open, even in the absence of solar wind entries, indicating that their formation does not require magnetic reconnection between the IMF and the magnetic anomalies (e.g., Diéval et al., 2015). We note that field-aligned diffusion indeed occurs whatever the field lines are open or closed. Furthermore, a heating source may further enhance the density structures by either causing an expansion of the neutral atmosphere (a given electron density level will rise in altitude) or by increasing the electron temperature leading to reduced recombination rates and thus larger plasma densities (Andrews et al., 2014). Diéval et al. (2015) based on their observations rejected the hypothesis that the dayside bulges are primarily driven by ionization/heating input from precipitating solar wind electrons, which had been proposed by earlier studies (Andrews et al., 2014, and references therein). However, solar wind precipitation and other processes may still contribute to strengthen existing density structures, as we will see below.

The status of the density structures changes as the planet rotates. The plasma density decreases due to electron-ion recombination when it enters the shadow. The nightside densities are often below 5,000 cm^{-3} (the lowest densities detectable by MARSIS AIS), so in practice seldom detectable (Němec et al., 2010). However, Němec, Morgan, Gurnett, and Brain (2011) have reported intermittent observations of elevated electron peak densities in areas of near-radial crustal fields with frequent open-field line topology during nighttime. They were detected via oblique echoes, indicating that these density structures were inclined plasma layers. Diéval et al. (2014) found that such cases of high peak densities on nightside tend to be observed simultaneously with precipitating tens to hundreds eV electrons (auroral or magnetotail), above the strong magnetic anomalies of the southern hemisphere, at times when the IMF points westward. Additional heating and ionization by energetic electron entries were thus necessary for the densities to become large enough to become detectable by MARSIS (Diéval et al., 2014; Němec, Morgan, Gurnett, & Brain, 2011). Diéval et al. (2015) postulated that a recurrent process independent from external conditions causes the density structures to reform during daytime in areas of near-radial crustal fields, and thereafter, they would disappear during nighttime due to plasma densities becoming too low to be measured. These

authors suggested that these structures would be sporadically enhanced at times of energetic electron precipitation driven by external conditions, making them observable by MARSIS. The observations reported here imply that this recurrent process involves transport (of plasma and/or of neutrals).

In general, the dayside electron densities at altitudes >300 km are greater in areas of crustal fields than in areas without (e.g., Andrews et al., 2013, 2015). At these high altitudes, the ionosphere is in the transport regime. This difference may occur due to a facilitated vertical transport of plasma along near-vertical crustal field lines, while such vertical transport is inhibited in areas where the IMF (nearly horizontal orientation on dayside; e.g., Brain et al., 2003) is free to permeate low altitudes. At the same time, the planetary plasma is trapped within the minimagnetospheres (e.g., Ramstad et al., 2016), where the solar wind seldom has access and can thus not trigger ion loss, which keeps plasma densities high. Similarly, plasma scale heights were found to be larger at 200–250 km altitudes, than at 150–200 km altitudes, in areas of near-radial crustal fields, due to the facilitated upward diffusion of plasma along the field lines (e.g., Ness et al., 2000).

There have been reports of sporadically elevated peak densities in areas of near-radial crustal fields on the dayside (Duru et al., 2016; Fallows et al., 2016, presented at DPS meeting #48; Nielsen, Fraenz, et al., 2007). We note that they are not necessarily related to the (recurrent) formation of density structures but may happen simultaneously and enhance the structures further. Nielsen, Fraenz, et al. (2007) found no simultaneous observations of precipitating plasma/X-ray flux able to explain cases of high densities at low altitude. They invoked the reduction of the electron-ion recombination rate due to Joule heating of atmospheric neutrals by AC electric fields related to plasma instabilities in areas of open crustal field lines. Finally, Duru et al. (2016) have observed, in an area of strong near-vertical crustal fields, a dayside case with simultaneous detection of: local plasma depletion at spacecraft altitude, peak density enhancement, and oblique echoes. They postulated that an earlier instance of magnetic reconnection between the crustal fields and the IMF allowed accelerated precipitating electrons to reach low altitudes along open field lines, providing heating and ionization that may have strengthened a density structure already present, and at the same time driving energization and outflow of planetary ions such as to form a density cavity at high altitude. They suggested that the increased peak electron density may have been caused by either the Nielsen, Fraenz, et al. (2007) mechanism or the electron precipitation.

We note that although the dayside oblique echoes are commonly observed above magnetic anomalies, plasma depletions and peak density enhancements are on the other hand rarely observed during daytime (Duru et al., 2016; Fallows et al., 2016, presented at DPS meeting #48; Hall et al., 2016). On the dayside, enhanced peak densities are found in areas of near-radial fields being more often open than usual and can be detected via oblique echoes (Fallows et al., 2016, presented at DPS meeting #48), similar to their nightside counterparts (Němec, Morgan, Gurnett, & Brain, 2011). From the Duru et al. (2016) case, we infer that whatever the shape distribution of the target of oblique echoes was when it formed, sporadic processes appear to have altered its shape distribution into presumably a dip at MEX location and a bulge near the ionospheric peak.

The methodology of the present work focuses on the study of time series of EDPs at selected frequencies to study horizontal density gradients. Another interesting way to study the topside ionosphere is to examine the vertical structure of the ionosphere, with single EDPs obtained either by inversion of ionograms or by radio occultation technique, to identify vertical density gradients (e.g., Kopf et al., 2008; Withers et al., 2005).

Withers et al. (2005) observed that density bumps and bite-outs can exist in regions of strong magnetic anomalies and that their occurrence seemed to depend on the crustal field inclination and azimuth. The altitudes of these features were found within the dynamo region of the Martian ionosphere, which exists between 120 and 190 km altitude for a magnetic field strength of 100 nT, as estimated by Withers et al. (2005). These authors suggested the role of neutral winds, magnetic field, and ionized plasma, within the dynamo region, to generate induced ionospheric currents and associated magnetic fields, which could modify the density profiles such as to create bite-outs or bumps. Field-aligned currents and Pedersen currents in magnetic cusp areas were simulated by, for example, Fillingim et al. (2010, 2012) and Riousset et al. (2013, 2014). Such currents are expected to always be present and can be a recurrent source of heating of the neutral atmosphere, localized to regions of magnetic cusps. Heating at altitudes below the ionospheric peak could cause the typically higher altitudes we have observed for the entire topside ionosphere in these regions.

Kopf et al. (2008) have discovered the existence of transient topside layers above the main ionospheric peak, at typical altitudes 180–240 km on the dayside, with an occurrence rate decreasing when going from the subsolar region to the terminator (from 60% to 5% of observation time). The topside layers are found mostly in regions of low crustal magnetic field strength (e.g., Kim et al., 2012; Kopf et al., 2017). It is not known whether topside layers exist in regions of stronger crustal fields, because the presence of electron cyclotron harmonics in the ionograms can hinder the visibility of the ionospheric traces at low frequency, including any potential topside layer. Concurrent measurements of topside layers by MARSIS onboard the MEX orbiter and by the in situ particle and field package onboard the MAVEN orbiter indicate localized increases in the in situ electron density and total ion density in the vicinity of the topside layers detected remotely by MARSIS (Kopf et al., 2017). These authors also found simultaneous magnetic field rotations and magnetic field dips, attributed to current sheets.

We remark that these topside layers have two characteristics that are incompatible with the characteristics of the density structures investigated in the present work: the former are transient and are detected away from regions of significant crustal fields (but could possibly exist in such regions although nondetectable due to cyclotron harmonics), while the latter reoccur regularly and only above regions of significant crustal fields. In addition, the former have been attributed to various mechanisms involving the solar wind interaction with the topside ionosphere (e.g., Kopf et al., 2017), while the latter seem to have no relationship to the upstream solar wind conditions or to the presence/absence of magnetosheath plasma entries at MEX altitude (e.g., Andrews et al., 2014; Diéval et al., 2015). Therefore, there seems to be no link between the topside layers and the regions giving oblique echoes. Another indication that these ionospheric features are independent is that topside layers can be present and give oblique echoes if found in areas where the main ionosphere layer already gives oblique echoes, but are not present otherwise (Venkateswara Rao et al., 2017).

Bulges may be the primary type of density structure to appear, as modeled in the simple case of vertical diffusion by Matta et al. (2015). They are the most observed simplest shape. Other shapes likely require more complex conditions. The formation of slopes may be related to gradients in the ability of the plasma to be transported, favoring convex slopes or concave slopes depending on circumstances. Dips possibly form as a result of ion outflow along open field lines at occasions of magnetic reconnection between the IMF and the crustal fields, during which the solar wind is able to energize the planetary ions within the minimagnetosphere. It is also possible that a magnetic arcade near the terminator possesses one footprint on dayside and the other footprint on nightside, such that electrons produced on dayside are lost on nightside after traveling along the arcade (e.g., Xu et al., 2016): this may cause a dip within the illuminated area of near-radial field lines. The restriction of our study to SZA $< 85°$ certainly limits the observation of this situation. Instead, we are working here with the commonly observed dayside events where both footprints of the corresponding magnetic arcades are reasonably expected to be illuminated. A decrease of the altitude level at selected frequencies could also be brought by the contracting and cooling of the underlying atmosphere, after a transient heating source (such as from solar wind precipitation) has subsided.

5. Summary

This paper reports a statistical study of oblique ionospheric echoes in the dayside Martian ionosphere identified with the MARSIS AIS radar data. The reflecting targets for these oblique echoes are nonhorizontal localized electron density structures associated to regions of near-radial crustal magnetic fields. The altitude variations (shape) of 48 density structure events corrected for signal dispersion have been investigated through time series of EDPs, by comparing a reference EDP (PI EDP) to the other EDPs in the same time series. We obtained the following results:

1. The altitude differences between the PI EDP and the edge EDPs tend to be larger at low frequencies (high altitudes) and smaller at high frequencies (low altitudes), with values going from a few tens of kilometers down to a few kilometers as frequency increases (equivalently altitude differences of a few tens of % down to a few % relative to the altitude of the PI EDP). The density structures are found with large-altitude variations in the region of transport regime (above ~200 km altitude) and with smaller altitude variations in the region of photochemistry regime (below ~200 km altitude).
2. The inspection of the hyperbola signatures in echograms at selected frequencies indicates that oblique echoes are more developed at low frequency than at high frequency, which is consistent with the

altitude differences between PI EDP and edges EDPs to be larger (more tilted density contour) at low frequency than at high frequency, and agrees with the result from Nielsen, Wang, et al. (2007).

3. There are four simplest possible shapes for inclined structures able to give oblique echoes: bulge, dip, uphill slope, and downhill slope. Uphill slopes and downhill slopes can be concave or convex. Convex slope events resemble dips (downward swell), and concave slope events resemble bulges (upward swells).
4. A given event may keep the same shape over all frequencies or change shape over frequency. The changes of shape over frequency are gradual, but systematic, with natural transitions between bulge and dip, separated by concave and convex slope events in the right order.
5. The comparison of the time series of EDPs at selected frequencies with the 1.8–2 MHz integrated echograms for individual events brings intriguing results. The apparent altitude of the apex of the hyperbola signature in the echograms does not vary consistently with the altitude levels corrected for dispersion: the apex of the hyperbola does not necessarily correspond to the highest (or lowest) real altitude level in the time series. The presence of one or two clear legs or short/unclear legs in the hyperbola signature does not seem to relate to the simplest shape in the EDP time series (it may be any of these: bulge, dip, downhill, and uphill slopes).
6. In most of the frequency range of the EDPs, the number of bulges dominates the numbers of other shapes. The number of bulges peaks at a fixed frequency 2.111 MHz, much higher than for the other shapes: the numbers of uphill slopes, downhill slopes, and dips peak at a fixed frequency of 1.63, 1.455, and 1.52 MHz, respectively.
7. At a given frequency, the altitude differences between the PI EDP and the edge EDPs tend to be larger in absolute value for bulges than for other shapes. It is possible that the smaller altitude differences of uphill slope, downhill slope, and dip events could be a bias from their small numbers. The median altitude difference we have determined for bulges at a fixed frequency 1.848 MHz is 12.4 km, which is of the same order as the rms apparent altitude of 19 km at a fixed frequency 1.8 MHz reported by Duru et al. (2006).
8. The examination of the entire frequency range of the EDPs in the time series of individual events indicates the possible presence of topside layers, density bumps, and density bite-outs (e.g., Kopf et al., 2008; Withers et al., 2005) in the form of slight ledges in the vertical structure. Also, the altitude level at a fixed frequency 1.936 MHz clearly increases when the ionospheric peak altitude increases, and has a weak increasing trend when the peak density increases. The entire topside ionosphere seems to move up and down in areas giving oblique echoes.
9. The latitude extension of the areas giving oblique echoes, which is usually comparable to the latitude extension of the corresponding magnetic cusps, permits a sampling of a wide range of crustal field orientations, from near-vertical up to near-horizontal. There is a tendency for more vertical crustal fields toward the center of the density structures, and more horizontal fields toward the edges.
10. At a fixed frequency 1.936 MHz, the relative altitude differences between the PI EDP and the other EDPs in the time series of individual events, and the classification into the four possible simplest shapes, seem to be independent or weakly dependent upon the crustal field orientation and vary for events located in geographical proximity (within 10° longitude) but detected at different dates and times.

Transport appears to be a key element in the formation of density structures. Two recurrent mechanisms based on transport could operate, possibly at the same time: (1) field-aligned diffusion of plasma along near-radial (open or closed) field lines and (2) electron density levels rising in altitude through the expansion of the ionizable neutral atmosphere presumably due to localized Joule heating by ionospheric currents at magnetic cusps. Other mechanisms may alter the density structures either by enhancing them or weakening them. Heating/ionization by electron precipitation or AC electric fields may further increase the plasma densities in areas of near-radial open crustal fields.

In-situ measurements in the altitude range of the density structures would be a valuable complement to the remote measurements enabled by MARSIS AIS. In particular, future studies making use of the rich combined capabilities of MEX and MAVEN would help understand the formation and evolution of individual structures; in particular, more in situ measurements of downhill slopes, uphill slopes and dips are, needed. Future studies also need to evaluate ray tracing of radio signals through models of ionospheric layers to study the

characteristics of oblique echoes; they would also be very useful to understand the intriguing results brought by the comparison of EDP time series and echograms.

Appendix A

The derived altitude profiles of Morgan et al. (2013) make two assumptions: vertical propagation and plane-parallel stratification. Here we discuss potential issues in applying these assumptions in regions of density structures. Morgan et al. (2013) warned about the use of the profiles in the areas of oblique echoes, because the assumption of vertical propagation may not be true. In fact, the single ionospheric echo received may be vertical or oblique depending on the density layer inclination at the reflection point. We note that MARSIS measures only the time delay to receive the echo, without knowledge of the angle between the echo direction and the nadir. This time delay is given as input to the inversion routine, which outputs the range corrected for dispersion. The inversion itself does not need the direction of the echo. It is only afterward, at the stage of calculating the altitude of the obtained profile that the assumption of vertical propagation is made: layer altitude = MEX altitude − layer range. Given that the reflection angle cannot be known, it is not possible to account for this angle to amend the layer altitude. Thus, in practice, we can only use the altitudes as derived with the nadir echo assumption. On the other hand, the assumption of plane-parallel stratification is applied inside the inversion routine and is thus required at an early stage to produce a range corrected for dispersion. Given the trend of the altitude differences PI EDP-edge EDP to increase over frequency (Figure 7), one may then wonder whether the density structures still respect a plane-parallel stratification over their whole frequency range. Below we check the validity of these two assumptions, for the events in our list, by using information from section 3.

We want to determine the angle that the inclined layer makes with the horizontal for different frequencies by considering a line joining the PI altitude and the edge altitude (beginning or end) and the angle between such successive inclined layers of consecutive frequencies. We care about how large the angles are, so we take their absolute values. In practice, it means changing all the events into bulges (absolute value of altitude differences for both edges), which is good for our purpose, especially since the majority of the events are bulges. Then we simplify the shape of the structures by keeping only the altitude variations of the edge EDPs and the PI EDP, ignoring the profiles in between, which effectively turns the shapes into triangles. Finally, we can calculate, for each frequency f, the angle α_f between a horizontal line at the altitude of the edge point and a line joining the altitudes of the edge and PI points: $\tan\alpha_f = H_f/D$. Here H_f is the absolute value of the altitude difference PI EDP-edge EDP at frequency f and D is the horizontal distance traveled by MEX between the edge and PI times (using the MEX velocity and the absolute value of the time difference between edge and PI). This is done separately for the beginning and end edges. Then we deduce the angle $\theta_{f2\ f1}$ between two successive inclined density layers of consecutive frequencies $f1$ and $f2$ ($f2 > f1$) as $\theta_{f2\ f1} = \alpha_{f2} - \alpha_{f1}$. As a remark, the density layer is very likely to be horizontal or near-horizontal both at the edge point (because it is very close to the surrounding normal ionosphere) and at the PI point (especially for a bulge or a dip), so we can use these altitude values directly, with the nadir echo assumption.

Figure A1 shows the distributions of the angle α_f (Figure A1a) and the angle $\theta_{f2\ f1}$ (Figure A1b), as a function of frequency, for all the events, for both the beginning and end edges, plotted as grey dots. The red dots correspond to the median angles versus frequency. Since α_f is proportional to H_f, the angle between horizontal and inclined layer tends to increase when the frequency decreases (Figure A1a), just like the altitude difference does increase. The distribution of angles broadens as frequency decreases, the angle increases from a few degrees at high frequency, up to ~15° at low frequency, confirmed by the increasing trend of the median values from 3.4 to 4.5°. Therefore, for these events, the inclined layers from the edge point to the PI point are weakly inclined to the horizontal, with angles typically small at all frequencies. Then, the distribution of $\theta_{f2\ f1}$ does not vary over frequency (Figure A1b), remaining close to zero at all frequencies: the angles between successive layers vary mostly up to 0.5°, with the median values remaining $\leq$0.1°. Therefore, these density layers are making negligible angles to each other at all frequencies, and basically appear as parallel strata from the edge point to the PI point. We conclude that for our list of density structures, the assumption of plane-parallel stratification is certainly valid, and the assumption of vertical reflection is,

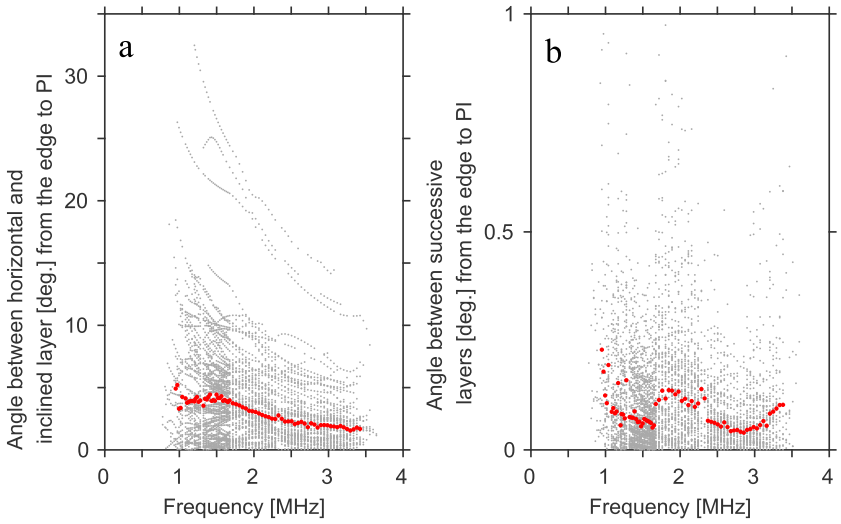

Figure A1. (a) Distribution of the angle between the horizontal and the inclined layer from the edge point to the PI point, versus frequency, for all the events, for both the beginning and end edges, plotted as grey dots. (b) Distribution of the angle between successive inclined layers (of consecutive frequencies), versus frequency, for all the events, plotted as grey dots. In both panels, the angles are shown in absolute value; the red dots indicate the median values versus frequency.

although no exactly true, good enough as approximation. Therefore, we are confident that these EDPs are valid and provide useful insight for these particular density structures.

For comparison, Nielsen, Wang, et al. (2007) estimated the angles of inclined layers to the vertical for a few cases of density structures, with a different hypothesis (assuming a fixed altitude for the reflection point), and found a wide range of values from 5 to 90°. We note that the assumption of vertical propagation is certainly not applicable for strongly inclined structures, and thus, the vertical profiles would be invalid in this case.

Acknowledgments
C. D. and J. A. W. were supported by grant ST/M001059/1 from the UK Science and Technology Facilities Council. A. J. K. was supported by NASA through contract 1560641 with the Jet Propulsion Laboratory. The MARSIS data are available on ftp://psa.esac.esa.int/pub/mirror/MARS-EXPRESS/MARSIS/. C. D. thanks F. Němec (e-mail address: frantisek.nemec@gmail.com) for providing updated MARSIS AIS EDPs.

References

Acuña, M. H., Connerney, J. E. P., Ness, N. F., Lin, R. P., Mitchell, D., Carlson, C. W., et al. (1999). Global distribution of crustal magnetization discovered by the Mars Global Surveyor MAG/ER experiment. *Science*, *284*(5415), 790–793. https://doi.org/10.1126/science.284.5415.790

Andrews, D. J., André, M., Opgenoorth, H. J., Edberg, N. J. T., Diéval, C., Duru, F., et al. (2014). Oblique reflections in the Mars Express MARSIS data set: Stable density structures in the Martian ionosphere. *Journal of Geophysical Research: Space Physics*, *119*, 3944–3960. https://doi.org/10.1002/2013JA019697

Andrews, D. J., Edberg, N. J. T., Eriksson, A. I., Gurnett, D. A., Morgan, D., Němec, F., & Opgenoorth, H. J. (2015). Control of the topside Martian ionosphere by crustal magnetic fields. *Journal of Geophysical Research: Space Physics*, *120*, 3042–3058. https://doi.org/10.1002/2014JA020703

Andrews, D. J., Opgenoorth, H. J., Edberg, N. J. T., André, M., Fränz, M., Dubinin, E., et al. (2013). Determination of local plasma densities with the MARSIS radar: Asymmetries in the high-altitude Martian ionosphere. *Journal of Geophysical Research: Space Physics*, *118*, 6228–6242. https://doi.org/10.1002/jgra.50593

Barabash, S., Lundin, R., Andersson, H., Brinkfeldt, K., Grigoriev, A., Gunell, H., et al. (2006). The Analyzer of Space Plasmas and Energetic Atoms (ASPERA-3) for the Mars Express mission. *Space Science Reviews*, *126*(1-4), 113–164. https://doi.org/10.1007/s11214-006-9124-8

Brain, D. A., Bagenal, F., Acuña, M. H., & Connerney, J. E. P. (2003). Martian magnetic morphology: Contributions from the solar wind and crust. *Journal of Geophysical Research*, *108*(A12), 1424. https://doi.org/10.1029/2002JA009482

Brain, D. A., Lillis, R. J., Mitchell, D. L., Halekas, J. S., & Lin, R. P. (2007). Electron pitch angle distributions as indicators of magnetic field topology near Mars. *Journal of Geophysical Research*, *112*, A09201. https://doi.org/10.1029/2007JA012435

Budden, K. G. (1961). *Radio waves in the ionosphere*. Cambridge, UK: Cambridge University Press.

Cain, J. C., Ferguson, B. B., & Mozzoni, D. (2003). An $n = 90$ internal potential function of the Martian crustal magnetic field. *Journal of Geophysical Research*, *108*(E2), 5008. https://doi.org/10.1029/2000JE001487

Diéval, C., Andrews, D. J., Morgan, D. D., Brain, D. A., & Gurnett, D. A. (2015). MARSIS remote sounding of localized density structures in the dayside Martian ionosphere: A study of controlling parameters. *Journal of Geophysical Research: Space Physics*, *120*, 8125–8145. https://doi.org/10.1002/2015JA021486

Diéval, C., Morgan, D. D., Němec, F., & Gurnett, D. A. (2014). MARSIS observations of the Martian nightside ionosphere dependence on solar wind conditions. *Journal of Geophysical Research: Space Physics*, *119*, 4077–4093. https://doi.org/10.1002/2014JA019788

Duru, F., Gurnett, D. A., Averkamp, T. F., Kirchner, D. L., Huff, R. L., Persoon, A. M., et al. (2006). Magnetically controlled structures in the ionosphere of Mars. *Journal of Geophysical Research*, *111*, A12204. https://doi.org/10.1029/2006JA011975

Duru, F., Gurnett, D. A., Diéval, C., Morgan, D. D., Pisa, D., & Lundin, R. (2016). A case study of a density structure over a vertical magnetic field region in the Martian ionosphere. *Geophysical Research Letters*, *43*, 4665–4672. https://doi.org/10.1002/2016GL068686

Duru, F., Morgan, D. D., & Gurnett, D. A. (2010). Overlapping ionospheric and surface echoes observed by the Mars Express radar sounder near the Martian terminator. *Geophysical Research Letters*, *37*, L23102. https://doi.org/10.1029/2010GL045859

Fallows, K., Withers, P., & Morgan, D. (2016). Oblique echoes at unusually high frequencies in MARSIS-AIS measurements of the topside ionosphere of Mars, American Astronomical Society, DPS meeting #48, id.220.33

Fillingim, M. O., Lillis, R. J., England, S. L., Peticolas, L. M., Brain, D. A., Halekas, J. S., et al. (2012). On wind-driven electrojets at magnetic cusps in the nightside ionosphere of Mars. *Earth, Planets and Space*, *64*(2), 93–103. https://doi.org/10.5047/eps.2011.04.010

Fillingim, M. O., Peticolas, L. M., Lillis, R. J., Brain, D. A., Halekas, J. S., Lummerzheim, D., & Bougher, S. W. (2010). Localized ionization patches in the nighttime ionosphere of Mars and their electrodynamic consequences. *Icarus*, *206*(1), 112–119. https://doi.org/10.1016/j.icarus.2009.03.005

Fox, J. L., & Yeager, K. E. (2006). Morphology of the near-terminator Martian ionosphere: A comparison of models and data. *Journal of Geophysical Research*, *111*, A10309. https://doi.org/10.1029/2006JA011697

Gurnett, D. A., Kirchner, D. L., Huff, R. L., Morgan, D. D., Persoon, A. M., Averkamp, T. F., et al. (2005). Radar soundings of the ionosphere of Mars. *Science*, *310*(5756), 1929–1933. https://doi.org/10.1126/science.1121868

Hall, B. E. S., Lester, M., Nichols, J. D., Sánchez-Cano, B., Andrews, D. J., Opgenoorth, H. J., & Fränz, M. (2016). A survey of superthermal electron flux depressions, or "electron holes," within the illuminated Martian induced magnetosphere. *Journal of Geophysical Research: Space Physics*, *121*, 4835–4857. https://doi.org/10.1002/2015JA021866

Hantsch, M. H., & Bauer, S. J. (1990). Solar control of the Mars ionosphere. *Planetary and Space Science*, *38*(4), 539–542. https://doi.org/10.1016/0032-0633(90)90146-H

Kim, E., Seo, H., Kim, J. H., Lee, J. H., Kim, Y. H., Choi, G. H., & Sim, E. S. (2012). The analysis of the topside additional layer of Martian ionosphere using MARSIS/Mars Express Data. *Journal of Astronomy and Space Sciences*, *29*(4), 337–342. https://doi.org/10.5140/JASS.2012.29.4.337

Kopf, A. J., Gurnett, D. A., DiBraccio, G. A., Morgan, D. D., & Halekas, J. S. (2017). The transient topside layer and associated current sheet in the ionosphere of Mars. *Journal of Geophysical Research: Space Physics*, *122*, 5579–5590. https://doi.org/10.1002/2016JA023591

Kopf, A. J., Gurnett, D. A., Morgan, D. D., & Kirchner, D. L. (2008). Transient layers in the topside ionosphere of Mars. *Geophysical Research Letters*, *35*, L17102. https://doi.org/10.1029/2008GL034948

Matta, M., Mendillo, M., Withers, P., & Morgan, D. (2015). Interpreting Mars ionospheric anomalies over crustal magnetic field regions using a 2-D ionospheric model. *Journal of Geophysical Research: Space Physics*, *120*, 766–777. https://doi.org/10.1002/2014JA020721

Morgan, D. D., Gurnett, D. A., Kirchner, D. L., Fox, J. L., Nielsen, E., & Plaut, J. J. (2008). Variation of the Martian ionospheric electron density from Mars Express radar soundings. *Journal of Geophysical Research*, *113*, A09303. https://doi.org/10.1029/2008JA013313

Morgan, D. D., Witasse, O., Nielsen, E., Gurnett, D. A., Duru, F., & Kirchner, D. L. (2013). The processing of electron density profiles from the Mars Express MARSIS topside sounder. *Radio Science*, *48*, 197–207. https://doi.org/10.1002/rds.20023

Nagy, A., Winterhalter, D., Sauer, K., Cravens, T. E., Brecht, S., Mazelle, C., et al. (2004). The plasma environment of Mars. *Space Science Reviews*, *111*(1/2), 33–114. https://doi.org/10.1023/B:SPAC.0000032718.47512.92

Němec, F., Morgan, D. D., & Gurnett, D. A. (2016). On improving the accuracy of electron density profiles obtained at high altitudes by the ionospheric sounder on the Mars Express spacecraft. *Journal of Geophysical Research: Space Physics*, *121*, 10,117–10,129. https://doi.org/10.1002/2016JA023054

Němec, F., Morgan, D. D., Gurnett, D. A., & Andrews, D. J. (2016). Empirical model of the Martian dayside ionosphere: Effects of crustal magnetic fields and solar ionizing flux at higher altitudes. *Journal of Geophysical Research: Space Physics*, *121*, 1760–1771. https://doi.org/10.1002/2015JA022060

Němec, F., Morgan, D. D., Gurnett, D. A., & Brain, D. A. (2011). Areas of enhanced ionization in the deep nightside ionosphere of Mars. *Journal of Geophysical Research*, *116*, E06006. https://doi.org/10.1029/2011JE003804

Němec, F., Morgan, D. D., Gurnett, D. A., & Duru, F. (2010). Nightside ionosphere of Mars: Radar soundings by the Mars Express spacecraft. *Journal of Geophysical Research*, *115*, E12009. https://doi.org/10.1029/2010JE003663

Němec, F., Morgan, D. D., Gurnett, D. A., Duru, F., & Truhlík, V. (2011). Dayside ionosphere of Mars: Empirical model based on data from the MARSIS instrument. *Journal of Geophysical Research*, *116*, E07003. https://doi.org/10.1029/2010JE003789

Ness, N. F., Acuña, M. H., Connerney, J. E. P., Kliore, A. J., Breus, T. K., Krymskii, A. M., et al. (2000). Effects of magnetic anomalies discovered at Mars on the structure of the Martian ionosphere and solar wind interaction as follows from radio occultation experiments. *Journal of Geophysical Research*, *105*, 15,991–16,004. https://doi.org/10.1029/1999JA000212

Nielsen, E., Fraenz, M., Zou, H., Wang, J.-S., Gurnett, D. A., Kirchner, D. L., et al. (2007). Local plasma processes and enhanced electron densities in the lower ionosphere in magnetic cusp regions on Mars. *Planetary and Space Science*, *55*(14), 2164–2172. https://doi.org/10.1016/j.pss.2007.07.003

Nielsen, E., Wang, X. D., Gurnett, D. A., Kirchner, D. L., Huff, R., Orosei, R., et al. (2007). Vertical sheets of dense plasma in the topside Martian ionosphere. *Journal of Geophysical Research*, *112*, E02003. https://doi.org/10.1029/2006JE002723

Picardi, G., Biccari, D., Seu, R., Plaut, J., Johnson, W. T. K., Jordan, R. L., et al. (2004). MARSIS: Mars Advanced Radar for Subsurface and Ionospheric Sounding. In A. Wilson (Ed.), *Mars Express: A European mission to the red planet* (pp. 51–69). Noordwijk, Netherlands: ESA Publications Division.

Ramstad, R., Barabash, S., Futaana, Y., Nilsson, H., & Holmström, M. (2016). Effects of the crustal magnetic fields on the Martian atmospheric ion escape rate. *Geophysical Research Letters*, *43*, 10,574–10,579. https://doi.org/10.1002/2016GL070135

Riousset, J. A., Paty, C. S., Lillis, R. J., Fillingim, M. O., England, S. L., Withers, P. G., & Hale, J. P. M. (2013). Three-dimensional multifluid modeling of atmospheric electrodynamics in Mars' dynamo region. *Journal of Geophysical Research: Space Physics*, *118*(6), 3647–3659. https://doi.org/10.1002/jgra.50328

Riousset, J. A., Paty, C. S., Lillis, R. J., Fillingim, M. O., England, S. L., Withers, P. G., & Hale, J. P. M. (2014). Electrodynamics of the Martian dynamo region near magnetic cusps and loops. *Geophysical Research Letters*, *41*, 1119–1125. https://doi.org/10.1002/2013GL059130

Sánchez-Cano, B., Lester, M., Witasse, O., Milan, S. E., Hall, B. E. S., Cartacci, M., et al. (2016). Solar cycle variations in the ionosphere of Mars as seen by multiple Mars Express data sets. *Journal of Geophysical Research: Space Physics*, *121*, 2547–2568. https://doi.org/10.1002/2015JA022281

Venkateswara Rao, N., Mohanamanasa, P., & Rao, S. V. B. (2017). Magnetically controlled density structures in the topside layer of the Martian ionosphere. *Journal of Geophysical Research: Space Physics*, *122*, 5619–5629. https://doi.org/10.1002/2016JA023545

Wang, J.-S., & Nielsen, E. (2003). Behavior of the Martian dayside electron density peak during global dust storms. *Planetary and Space Science*, *51*(4-5), 329–338. https://doi.org/10.1016/S0032-0633(03)00015-1

Wang, X.-D., Wang, J. S., Nielsen, E., & Zou, H. (2009). "Hook" structure in MARSIS ionogram and its interpretation. *Geophysical Research Letters*, *36*, L13103. https://doi.org/10.1029/2009GL038844

Withers, P., Mendillo, M. J., Rishbeth, H., Hinson, D. P., & Arkani-Hamed, J. (2005). Ionospheric characteristics above Martian crustal magnetic anomalies. *Geophysical Research Letters*, *32*, L16204. https://doi.org/10.1029/2005GL023483

Withers, P., Weiner, S., & Ferreri, N. R. (2015). Recovery and validation of Mars ionospheric electron density profiles from Mariner 9. *Earth, Planets and Space*, *67*(1), 67–194. https://doi.org/10.1186/s40623-015-0364-2

Xu, S., Mitchell, D., Liemohn, M., Dong, C., Bougher, S., Fillingim, M., et al. (2016). Deep nightside photoelectron observations by MAVEN SWEA: Implications for Martian northern hemispheric magnetic topology and nightside ionosphere source. *Geophysical Research Letters*, *43*, 8876–8884. https://doi.org/10.1002/2016GL070527